

# Recovering the Tidal Field in the Projected Galaxy Distribution

David Alonso<sup>1\*</sup>, Boryana Hadzhiyska<sup>2†</sup>, Michael A. Strauss<sup>2‡</sup>

<sup>1</sup>*University of Oxford, Denys Wilkinson Building, Keble Road, Oxford, OX1 3RH, UK*

<sup>2</sup>*Department of Astrophysical Sciences, Princeton University, Princeton, NJ 08544 USA*

11 December 2015

## ABSTRACT

We present a method to recover and study the projected gravitational tidal forces from a galaxy survey containing little or no redshift information. The method and the physical interpretation of the recovered tidal maps as a tracer of the cosmic web are described in detail. We first apply the method to a simulated galaxy survey and study the accuracy with which the cosmic web can be recovered in the presence of different observational effects, showing that the projected tidal field can be estimated with reasonable precision over large regions of the sky. We then apply our method to the 2MASS survey and present a publicly available full-sky map of the projected tidal forces in the local Universe. As an example of an application of these data we further study the distribution of galaxy luminosities across the different elements of the cosmic web, finding that, while more luminous objects are found preferentially in the most dense environments, there is no further segregation by tidal environment.

**Key words:** cosmology: large-scale structure of the Universe – cosmology: observations

## 1 INTRODUCTION

The nature of environmental effects in structure formation is an important field of study, both in astrophysics and cosmology. The dependence of halo and galaxy abundances on environmental density, for instance, gives rise to the bias relation linking the halo/galaxy distribution to the true matter density (Mo & White 1996; Sheth & Tormen 1999), and represents a central issue in the road to maximizing the amount of information that can be extracted from galaxy clustering analyses. Likewise, the environmental tidal forces are expected to distort the intrinsic shapes and alignments of galaxies, and therefore this effect must be correctly understood in order to obtain unbiased results from weak lensing studies (Catelan et al. 2001; Hirata & Seljak 2004).

Although the study of environmental effects has traditionally been focused on the impact of the environmental density, in recent years many groups have studied the effect of other quantities, such as the morphology of the environmental density field, the local tidal forces or the velocity field (Sousbie et al. 2008; Forero-Romero et al. 2009; Bond et al. 2010b; Hoffman et al. 2012). Each of these quantities can be used to define a different classification scheme of environment types in order to describe the statistics of

the so-called “cosmic web”: i.e. the arrangement of the matter distribution into interconnected structures of different dimensionality (Bond & Myers 1996). Although the use of these additional observables undoubtedly furthers our understanding of environmental effects in structure formation, these quantities themselves may also contain relevant cosmological information.

There has been extensive work in quantifying and understanding the properties of the cosmic web from N-body simulations, as well as its interplay with various intrinsic halo and galaxy properties (Hahn et al. 2007; Yan et al. 2013; Forero-Romero et al. 2014; Libeskind et al. 2014; Nuza et al. 2014; Metuki et al. 2015) and a smaller number of groups have attempted similar studies on galaxy survey data (Bond et al. 2010a; Eardley et al. 2015; Chen et al. 2015). Often this is done by using the galaxy number density in redshift space as a proxy for the real-space matter density. However this approach entails a number of difficulties, such as the theoretical uncertainty in the relationship between galaxies and dark matter or the presence of redshift-space distortions. Furthermore, it is often difficult to measure accurate redshifts for a sufficiently large number of sources (e.g. very faint galaxies) and, although one can resort to the use of photometric redshifts, the lack of precise radial information precludes any attempt at an accurate reconstruction of the three-dimensional density field necessary to study the cosmic web. In these cases, however, there is

\* E-mail: david.alonso@astro.ox.ac.uk

† E-mail: boryanah@princeton.edu

‡ E-mail: strauss@astro.princeton.edu

still a significant amount of information encoded in the projected two-dimensional galaxy distribution, which could potentially be used to study the statistics of the cosmic web. In this work we present a method to carry out this kind of analysis, which we then implement on the Two Micron All-Sky Survey (2MASS hereafter (Skrutskie et al. 2006)), a low-redshift imaging catalog, to produce a full-sky map of the projected tidal forces in the local Universe.

This paper is structured as follows. In section 2 we present our method as a two-dimensional implementation of the cosmic web classification based on the tidal tensor, and interpret the recovered observable in terms of the projected transverse tidal forces. We validate this method in Section 3 by implementing it on an N-body-based sythetic galaxy catalog, and devise a technique to deal with an incomplete sky coverage. The implementation of the method on the 2MASS survey is presented in Section 4. As a proof of concept we also use the produced maps of the projected tidal field to study the dependence of the luminosity function on the tidal classification of the environment. Our conclusions are presented in Section 5.

## 2 THE 2D TIDAL TENSOR AND THE PROJECTED COSMIC WEB

### 2.1 The three-dimensional tidal tensor

One of the most popular methods used in the literature to study the properties of the cosmic web is through the structure of the gravitational tidal forces (Doroshkevich 1970; Hahn et al. 2007; Forero-Romero et al. 2009). The action of these forces on an extended body of size  $l$  stretches or contracts it along different directions based on the structure of the Hessian of the gravitational potential  $\bar{\Phi}$ , also called the tidal tensor field:

$$\ddot{l}_i = -l_j \partial_j \partial_i \bar{\Phi}. \quad (1)$$

The tidal tensor is symmetric, and therefore can always be diagonalised at any point in space by performing a three-dimensional rotation. The eigenvalues of the tidal tensor therefore inform us about the strength of the tidal forces in three independent orthogonal directions, and their sign can be used to classify four different types of environments. In the standard cosmic web classification, at a point in space in which all the eigenvalues are positive, extended objects will be compressed in all directions, and such a point is classified as a *knot*. On the other end, objects in a region where the tidal field has all-negative eigenvalues will be stretched in all directions, and the region is classified as a *void*. The intermediate cases correspond to filaments (two positive and one negative eigenvalues) and sheets (one positive and two negative eigenvalues).

Note that, even though this nomenclature alludes to the geometrical or morphological properties of these structures, the method is entirely based on the properties of the tidal field, and thus is dynamical in nature. This is different from the alternative approach of separating distinct elements of the cosmic web in terms of the morphology of the density field (e.g. Bond et al. (2010a)). An added value of dynamical prescriptions is the direct physical interpretation of the resulting structures in terms of contracting and expanding

directions, which can have a direct impact on the physics of galaxy formation. Other similar methods based on the tidal tensor or the velocity shear tensor have been proposed in the literature Sousbie et al. (2008); Bond et al. (2010a); Hoffman et al. (2012); Libeskind et al. (2013) following a similar rationale.

Here we will adhere to the formalism used in Forero-Romero et al. (2009); Alonso et al. (2015). For simplicity we will work with a rescaled version of the Newtonian potential:  $\Phi \equiv \bar{\Phi}/(4\pi G\bar{\rho})$ , for which the Poisson equation is simply  $\nabla^2 \Phi = \Delta$ , where  $\Delta$  is the matter overdensity field. We then define the tidal tensor field as  $T_{ij} = \partial_i \partial_j \Phi$ , so that  $\Delta = \text{Tr}(\hat{T})$ , and we will classify the environment according to the number of eigenvalues  $\alpha$  above a given threshold  $\Lambda_{\text{th}}$  (not necessarily  $\Lambda_{\text{th}} = 0$ ). The standard approach to compute the tidal tensor in three-dimensional datasets is to first estimate the gravitational potential  $\Phi$  by solving Poisson's equation in Fourier space, and then differentiate it (also in Fourier space) to compute its Hessian. Thus, the Fourier transforms of the tidal tensor and the three-dimensional density field are related through

$$T_{ij}(\mathbf{k}) = \frac{k_i k_j}{k^2} \Delta(\mathbf{k}). \quad (2)$$

The density field used for these analyses is usually smoothed down to a given scale  $R_s$ , either to mitigate shot-noise, filter out non-linear effects or in order to study the scale-dependence of the resulting tidal field. We will do the same in the 2-dimensional case.

### 2.2 The 2D tidal tensor

#### 2.2.1 Definition

The formalism introduced above is straightforward to implement in an N-body simulation, and methods have been devised to use it also in spectroscopic galaxy catalogues (e.g. Bond et al. (2010b); Choi et al. (2010); Eardley et al. (2015)), where three-dimensional positions can be accurately determined for all galaxies (at least up to the effect of peculiar velocities). However, determining accurate spectroscopic redshifts for individual galaxies is a very time-consuming operation, and often in astronomy we are forced to make do with datasets for which radial positions are very poorly measured, as is the case for photometric redshift surveys, or even completely unknown. While a large amount of information is lost in the absence of accurate radial positions, a sizeable portion of it still remains encoded in the projected angular distribution of galaxies. The method presented here is intended to enable the study of environmental tidal forces in the matter distribution in these cases.

The idea behind this method is to use a straightforward dictionary between three-dimensional and two-dimensional projected quantities. A proxy of the transverse components (i.e. perpendicular to the line of sight) of the projected tidal tensor is computed from the projected density field using the following prescription:

- The direct observable in a projected dataset is the projected overdensity  $\delta(\hat{\mathbf{n}})$ : the fluctuations in the angular number density of galaxies with respect to the mean. This is related to the three-dimensional overdensity field  $\Delta(\mathbf{x})$

through a line-of-sight projection:

$$\delta(\hat{\mathbf{n}}) = \int_0^\infty d\chi w(\chi) \Delta_s(\chi \hat{\mathbf{n}}), \quad (3)$$

where  $\chi$  is the comoving radial distance,  $w(\chi)$  is the survey selection function and  $\Delta_s(\mathbf{x})$  is the redshift-space three-dimensional overdensity field. Here and in what follows we will denote all projected quantities using the lower-case version of the symbols used for the analogous three-dimensional objects.

As mentioned in the previous section, we filter out the smallest scales of the density field to mitigate shot-noise effects and non-linearities. For this we will use a Gaussian smoothing kernel defined by its standard deviation  $\theta_s$ .

- We define the 2D potential  $\phi$  as the solution to Poisson's equation on the sphere with  $\delta$  as a source:

$$\nabla_{\hat{\mathbf{n}}}^2 \phi \equiv \delta, \quad (4)$$

where  $\nabla_{\hat{\mathbf{n}}}^2 \equiv \partial_\theta^2 + \partial_\varphi^2 / \sin^2 \theta + \cot \theta \partial_\theta$  is the covariant Laplacian on the sphere, and  $\theta$  and  $\varphi$  are the elevation and azimuthal spherical coordinates respectively. Note that  $\phi$  thus defined is not the same as the projected potential  $\tilde{\phi}$ , given by

$$\tilde{\phi}(\hat{\mathbf{n}}) \equiv \int_0^\infty d\chi w(\chi) \Phi(\chi \hat{\mathbf{n}}). \quad (5)$$

We will discuss these differences in more detail in Sections 2.2.2, 3.3 and Appendix C.

- The 2D tidal tensor  $t_{ab}$  is then defined as the covariant Hessian of the 2D potential,  $t_{ab} \equiv H_{ab} \phi$ , where the covariant Hessian operator is given by

$$\hat{H} \equiv \begin{pmatrix} \partial_\theta^2 & \partial_\theta(\partial_\varphi / \sin \theta) \\ \partial_\theta(\partial_\varphi / \sin \theta) & \partial_\varphi^2 / \sin^2 \theta + \cot \theta \partial_\theta \end{pmatrix}. \quad (6)$$

The procedure outlined above is nothing but a direct analogy with what is done to obtain the three-dimensional tidal tensor: find the potential by solving Poisson's equation using Fourier methods and then compute the second derivatives of that potential. Although this is a simple way to define the 2D tidal tensor, we must first understand the physical interpretation of the object thus computed. We do so in the next section.

### 2.2.2 Physical interpretation of the 2D tidal tensor

The physical interpretation of the 2D tidal tensor introduced in the previous section is most easily understood in the flat-sky approximation. In this case, the projected overdensity is related to the three-dimensional one through:

$$\delta(\mathbf{x}) \equiv \int dz w(z) \Delta_s(\mathbf{x}, z). \quad (7)$$

Here  $\mathbf{x} = (x, y)$  are the coordinates perpendicular to the line of sight, and we have chosen  $z$  to be the radial coordinate.  $\Delta_s(\mathbf{x}, z)$  is the three-dimensional overdensity field in redshift-space, and  $w(z)$  is the radial selection function.

It is easy to relate  $\delta(\mathbf{x})$  to the Fourier transform of the 3D matter overdensity field:

$$\delta(\mathbf{x}) = \int \frac{dk^2}{2\pi} e^{i\mathbf{k}\mathbf{x}} \int dq w(q) b \left[ 1 + \beta \frac{q^2}{k^2 + q^2} \right] \Delta(\mathbf{k}, q), \quad (8)$$

where  $\mathbf{k}$  and  $q$  are the components of the wave vector perpendicular and parallel to the line of sight respectively, and  $w(q)$  is the Fourier transform of the selection function

$$w(q) \equiv \int \frac{dz}{\sqrt{2\pi}} w(z) e^{iqz}. \quad (9)$$

The factors  $b$  and  $\beta$  in Eq. 8 account for the galaxy bias and linear redshift-space distortions (i.e.  $\beta \equiv f/b$ , where  $f \equiv d \log D / d \log a$  is the linear growth rate).

According to the definition used in the previous section, the 2D tidal tensor  $\hat{t}$  and its three-dimensional version  $\hat{T}$  along the two transverse directions are related to the projected and three-dimensional density fields in Fourier space respectively through

$$t_{ab} \equiv \frac{k_a k_b}{k^2} \delta(\mathbf{k}), \quad T_{ab} \equiv \frac{k_a k_b}{k^2 + q^2} \Delta(\mathbf{k}, q), \quad (10)$$

and thus, they are related to each other through

$$t_{ab}(\mathbf{x}) = b \int \frac{dk^2}{2\pi} e^{i\mathbf{k}\mathbf{x}} \int dq \omega(q, k) T_{ab}(\mathbf{k}, q), \quad (11)$$

where we have defined the modified selection function:

$$\omega(q, k) \equiv w(q) \left[ 1 + (1 + \beta) \frac{q^2}{k^2} \right], \quad (12)$$

On the other hand, the transverse components of the three-dimensional tidal tensor projected along the line of sight are given by

$$\tilde{t}_{ab}(\mathbf{x}) \equiv \int \frac{dk^2}{2\pi} e^{i\mathbf{k}\mathbf{x}} \int dq w(q) T_{ab}(\mathbf{k}, q). \quad (13)$$

Comparing Equations 11 and 13 we can see that the differences between both quantities are fully encapsulated in the different selection functions  $w$  and  $\omega^1$ .

Typically, the selection function  $w$  of any survey will have a characteristic radial width  $l_z$ , and therefore its Fourier transform will have support over a range of scales  $q \lesssim 1/l_z$  (e.g., the Fourier transform of a Gaussian selection function with variance  $l_z$  is a Gaussian with variance  $1/l_z$ ). Since  $\omega$  and  $w$  differ significantly only for values of  $q \gtrsim k$  (we assume that the RSD parameter  $\beta$  is  $O(1)$ ), this implies that, as long as we focus only on angular scales  $k \gtrsim 1/l_z$ , the 2D tidal tensor  $t_{ab}$  and the projected tidal tensor  $\tilde{t}_{ab}$  will be proportional to each other to a very good approximation.

Hence, for sufficiently wide window functions,  $t_{ab}$  can be safely interpreted on all scales of interest as the magnitude of the tidal forces in the transverse directions averaged along the line of sight over the survey selection function. A more rigorous and quantitative proof of this result using a full-sky formalism is presented in Appendix C, and we demonstrate it in practice in Section 3.3.

### 2.2.3 Classification of the projected cosmic web

Bearing in mind the physical interpretation of the 2D tidal tensor, we can now justify an environmental classification based on it. We thus define three different types of environments in terms of the number of eigenvalues of the 2D tidal tensor larger than a given eigenvalue threshold  $\lambda_{\text{th}}$ . We

<sup>1</sup> as well as the multiplicative galaxy bias factor  $b$ , due to the fact that the true tidal field is caused by the total matter density.

chose to retain the names *knots* and *voids* to denote regions in which both or none of the eigenvalues exceed the threshold respectively, and we label any region in which only one of the eigenvalues is found above the threshold as a *nexus*. In what follows we will order the two eigenvalues of the 2D tidal tensor have so that  $\lambda_1 \geq \lambda_2$ , and therefore our prescription for the tidal classification reads:

- (i) **Void**: all eigenvalues below the threshold ( $\lambda_1 \leq \lambda_{\text{th}}$ ).
- (ii) **Nexus**: only 1 eigenvalue above the threshold ( $\lambda_2 \leq \lambda_{\text{th}} < \lambda_1$ ).
- (iii) **Knot**: all eigenvalues above the threshold ( $\lambda_{\text{th}} \leq \lambda_2$ ).

This formalism has one free parameter: the eigenvalue threshold  $\lambda_{\text{th}}$ . In the three-dimensional case, several prescriptions have been proposed in the literature to choose a value for the analogous parameter  $\Lambda_{\text{th}}$ . A choice of  $\Lambda_{\text{th}} = 0$  would separate different regions based purely on the direction of the tidal forces. This prescription would assume that gravitational collapse is underway along a given direction even if the eigenvalue is only infinitesimally positive, although in this case collapse would only occur after a very long time. This prescription thus produces a tidal classification in which voids occupy only about  $\sim 20\%$  of the volume, in striking contrast with the visual impression from redshift surveys and N-body simulations that most of the volume is actually empty. A choice of  $\Lambda_{\text{th}} > 0$  would therefore only regard a given direction as “collapsing” if the tidal forces are sufficiently strong, and would give rise to a tidal classification in which the abundance of voids better matches our intuitive expectations. The spherical collapse model would suggest an appropriate value for  $\Lambda_{\text{th}} \sim O(1)$  [Forero-Romero et al. \(2009\)](#), which would actually classify a large fraction of regions with overdensities  $\delta \gtrsim 1$  as voids. This is partly due to the failure of the spherical collapse model to describe the physics of anisotropic collapse, and therefore an intermediate value of  $\Lambda_{\text{th}}$  is sometimes chosen in order to produce the correct visual impression of the cosmic web classification.

In order to avoid this arbitrariness we have followed a prescription similar to the one proposed by [Eardley et al. \(2015\)](#): for different values of the eigenvalue threshold we calculate the number of galaxies in the survey located in the three different environmental types, and we choose the value of  $\lambda_{\text{th}}$  that most equally divides the galaxy population among the different types, thus minimizing the statistical uncertainty when studying the statistics of the galaxy population in all the environments simultaneously. The exact procedure we used to select a value for  $\lambda_{\text{th}}$  is the following: for the three environment types: ( $\alpha = (0, 1, 2)$ ) we compute the fraction of galaxies in it:  $F_\alpha = N_\alpha / N_{\text{total}}$ . We then compute the root-mean-square deviation in these fractions as:

$$\Sigma_F = \frac{1}{3} \sqrt{\sum_{\alpha=0}^2 \left(F_\alpha - \frac{1}{3}\right)^2}, \quad (14)$$

and select the value of  $\lambda_{\text{th}}$  that minimizes  $\Sigma_F$ . The actual value of  $\lambda_{\text{th}}$  depends on the smoothing scale used as well as on the galaxy population under study. As shown in Section 4.2, for our fiducial smoothing scale of  $1^\circ$  and the 2MASS sample, the optimal value is  $\lambda_{\text{th}} = 0.05$ . Note that, although this criterion maximizes the statistics in the three environments simultaneously, it is not necessarily the optimal choice

in order to enhance possible tidal effects in the galaxy distribution.

### 3 TESTING THE METHOD ON SIMULATED DATASETS

#### 3.1 Simulations

We have first tested the method to estimate the 2D tidal tensor on a simulated galaxy catalog in order to rigorously verify the different systematic effects that could contaminate the measurements in the real data. The simulated data will also allow us to evaluate the agreement of these measurements with our theoretical expectations.

Our target galaxy catalog is the 2MASS survey, described in Section 4.1, and therefore we generated the simulated catalog to match 2MASS in terms of number density, clustering amplitude and redshift and magnitude distributions. The base of our simulated survey is a dark-matter-only N-body simulation, produced by the hybrid TreePM code *Gadget-2* [Springel \(2005\)](#). It was run on a cubic box of size  $L_{\text{box}} = 700 \text{ Mpc}/h$  containing  $1024^3$  particles with a particle mass  $m_p = 2.7 \times 10^{10} M_\odot/h$ . This mass resolution was necessary to populate the dark-matter haloes with galaxies matching the redshift and magnitude distributions of 2MASS. The simulation was run assuming a flat  $\Lambda$ CDM cosmology with cosmological parameters  $(\Omega_M, \Omega_b, h, \sigma_8, n_s) = (0.3, 0.05, 0.7, 0.8, 0.96)$ , in approximate agreement with [Planck Collaboration et al. \(2014\)](#). The initial conditions for the simulation were generated at redshift  $z_{\text{ini}} = 49$  using second-order Lagrangian perturbation theory with a matter transfer function computed by the Boltzmann code *CAMB* [Lewis et al. \(2000\)](#) for the cosmological parameters above.

A comoving snapshot of the simulation at redshift  $z = 0.1$  (the median redshift of 2MASS) was used to generate the mock galaxy catalog. First, a halo catalog was generated using a Friends-of-Friends (FoF) code<sup>2</sup> with a linking length of  $b = 0.2$  in units of the mean interparticle distance of the simulation. All haloes containing 5 or more particles were included in the catalog. Although it is not clear whether FoF groups with such a small number of particles can describe virialized structures accurately, the main aim of this catalog is not to study the galaxy-halo relationship accurately, but rather to produce a galaxy sample that matches the statistical properties of 2MASS, which we have managed to accomplish. Furthermore, haloes with masses below 5 particles are only needed to reach survey completeness at the smallest redshifts ( $z \lesssim 0.03$ ), and therefore the impact of the galaxies populating those haloes on the statistics of the overall sample is almost negligible.

Haloes were populated with galaxies following a simplified version of the hybrid method proposed in [Carretero et al. \(2015\)](#), combining Halo Abundance Matching (HAM) [Vale & Ostriker \(2004\)](#) and Halo Occupation Distribution (HOD) [Peacock & Smith \(2000\)](#); [Berlind & Weinberg \(2002\)](#) techniques. All haloes with masses larger than a threshold

<sup>2</sup> The halo finder is publicly available and can be found at <https://github.com/damonge/MatchMaker>.



$M_{\min}$  were assigned a single central galaxy, and a mass-dependent average number of satellite galaxies given by

$$\langle N_{\text{sat}}(M) \rangle = \left( \frac{M}{M_1} \right)^\beta, \quad (15)$$

and all haloes below  $M_{\min}$  were left empty. The actual number of satellite galaxies assigned to each halo was drawn from a Poisson distribution with this mean. In order to assign luminosities to each galaxy following the 2MASS luminosity function we first related halo masses to luminosities by matching the cumulative luminosity function and the cumulative galaxy number density as a function of halo mass. Specifically, halo masses ( $M_h$ ) were related to  $K_s$ -band luminosities ( $L_K$ ) by solving the equation:

$$\int_{L_K}^{\infty} dL \frac{dn_g}{dL} = \int_{M_h}^{\infty} dM n(M) [1 + \langle N_{\text{sat}}(M) \rangle] \quad (16)$$

where  $dn_g/dL$  is the  $K_s$ -band luminosity function and  $n(M)$  is the halo mass function. For the mass function we chose the parametrization by Jenkins et al. (2001), which we found matches the halo mass distribution in our simulation to good accuracy. For the luminosity function we used the measurements of Appleby & Shafieloo (2014) at  $K_s < 13.5$ , in which  $dn_g/dL$  is modelled as a Schechter function with parameters  $\phi^* = 1.10 \times 10^{-2} (\text{Mpc}/h)^{-3}$ ,  $M_K^* = -23.52 + 5 \log(h)$  and  $\alpha = -1.00$ .

Once the  $M_h - L_K$  relation is found, central galaxies are assigned the luminosity corresponding to the host halo mass, and satellites are given a luminosity drawn from the satellite luminosity function, given in its cumulative form by

$$n_{\text{sat}}(> L_K) \equiv \int_{L_K}^{\infty} dL \frac{dn_g}{dL} - \int_{M_h(L_K)}^{\infty} dM n(M). \quad (17)$$

This algorithm guarantees that the resulting galaxy sample will follow the input luminosity function. Once intrinsic luminosities were assigned, the apparent  $K_s$  magnitude was computed for each galaxy using Eq. 31, and a cut  $K_s \geq 13.9$  (corresponding to the 2MASS completeness limit) was imposed.

The three free parameters of this method,  $M_{\min}$ ,  $M_1$  and  $\beta$  were fixed by matching the amplitude of the angular power spectrum in the simulation to that of the 2MASS data for three galaxy samples with different limit magnitudes:  $K_s < 13.5$ ,  $K_s < 13.8$  and  $K_s < 13.9$ . We found the combination  $\log_{10}[M_{\min}/(M_{\odot}/h)] = 10.7$ ,  $\log_{10}[M_1/(M_{\odot}/h)] = 13.5$  and  $\beta = 1.4$  to yield a good agreement with the data in terms of clustering amplitude, number density and redshift distribution.

Finally, we must note that the size of the simulation box is not quite large enough to encompass the whole volume covered by 2MASS. In order to achieve the required volume we replicated the box once in each of the three dimensions, making use of the periodic boundary conditions of the simulation. This implies that our simulated catalog lacks all clustering modes larger or similar to the size of the simulation box (700 Mpc/h), which is irrelevant for the scales used in the comparison of the mock catalog with our 2MASS sample. The redshift distribution of our simulated catalog is shown in Fig. 1 together with the corresponding one for 2MASS, extracted from the spectroscopic sample described in Section 4.2.3.

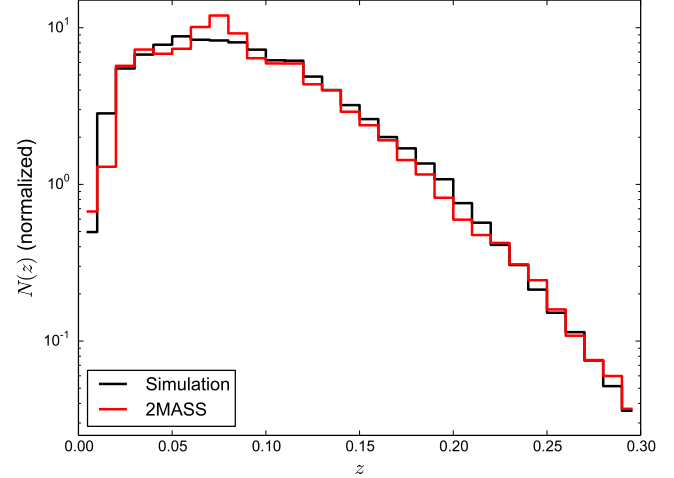


**Figure 1.** Redshift distribution of the simulated galaxy catalog (black) and the sample of 2MASS galaxies with  $K_s < 13.9$  used in this analysis (red). The latter was estimated from the redshifts of the complete spectroscopic sample in the northern galactic hemisphere, comprising  $\sim 113000$  objects (see Section 4.2.3). Both histograms have been normalized to unit area.

### 3.2 Statistics of the projected cosmic web

We first study the 2D tidal tensor and the projected cosmic web classification for the sample of galaxies in our simulated catalog matching the fiducial sample used in the analysis of the 2MASS data, comprised of all galaxies with apparent magnitudes  $K_s < 13.9$ . For this sample we carry out the steps outlined in Section 2.2.1.

(i) Throughout the analysis we use the HEALPix pixelization scheme Górski et al. (2005) with a resolution parameter  $N_{\text{side}} = 64$ , corresponding to pixels with an area of  $\sim 0.84 \text{ deg}^2$ . Given the number density of sources in 2MASS, higher resolution parameters would yield an estimate of the density field overly dominated by shot noise.

(ii) We compute the overdensity field in the full sky by counting the number of galaxies in each pixel  $N_p$  and dividing by the average number of galaxies per pixel  $\bar{N}$ . The field in pixel  $p$  is then given by:

$$\delta_p = \frac{N_p}{\bar{N}} - 1. \quad (18)$$

(iii) Since our method to compute the 2D tidal tensor involves the numerical differentiation of the 2D potential  $\phi$ , in order to suppress the numerical noise in the computation of those derivatives we first smooth the overdensity field using a Gaussian smoothing kernel, with standard deviation  $\theta_{\text{sm}} = 1^\circ$  and  $5^\circ$ . At the median redshift of our simulation ( $\bar{z} \sim 0.08$ ) these angles correspond to physical scales of 4.4 and 31.2 Mpc/h respectively. The use of different smoothing scales also allows us to study the properties of the cosmic web as a function of scale, which will be useful in order to compare our results with the linear theory outlined in Appendix B.

(iv) The 2D potential  $\phi$ , as described by Eq. 4, is computed from the smoothed density field  $\delta$  by solving Poisson's equation on the sphere. This is trivially done in harmonic space, since the harmonic coefficients of the two quantities

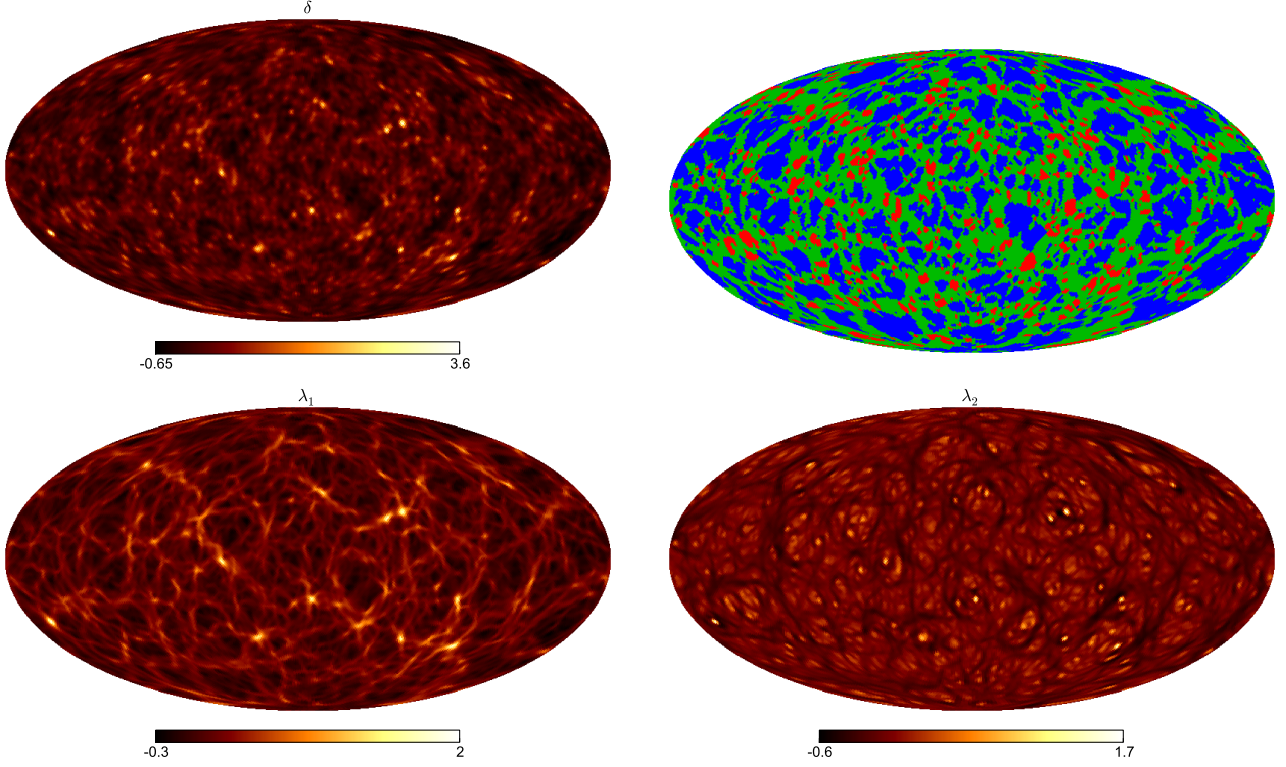


**Figure 2.** *Top left panel:* density field of the simulated galaxy catalog smoothed with a  $1^\circ$  Gaussian kernel. *Top right panel:* environment classification for the fiducial threshold  $\lambda_{\text{th}} = 0.05$ , with knots, nexuses and voids shown in red, green and blue respectively. *Bottom panels:* full-sky maps of the two eigenvalues of the 2D tidal tensor.

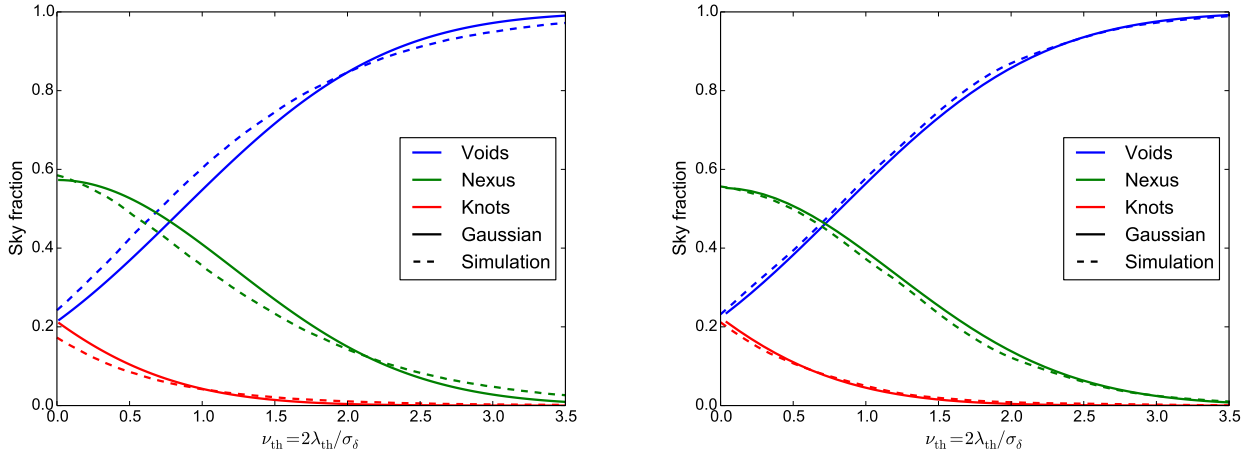


**Figure 3.** Gaussian prediction for the sky fraction each environment occupies as a function of the ratio of the eigenvalue threshold and the standard deviation of the projected overdensity field (solid), compared with the sky fractions in the simulated data (dashed). The smoothing angle is  $\theta_{\text{sm}} = 1^\circ$  for the left panel and  $\theta_{\text{sm}} = 5^\circ$  for the right one. The effects of non-linearities are significantly reduced for the larger smoothing scale, and the measured sky fractions agree better with the Gaussian prediction.

are proportional to each other:

$$\phi_{\ell m} = -\frac{\delta_{\ell m}}{\ell(\ell+1)}. \quad (19)$$

(v) The 2D tidal tensor is then computed by differentiating the 2D potential as in Eq. 6. The covariant Hessian was computed using the routines provided by the HEALPix

python package `healpy`<sup>3</sup>, which perform the derivatives in harmonic space. The estimated tidal tensor in each pixel is then diagonalized, and the values of the two eigenvalues are used to classify each pixel as belonging to one of the three

<sup>3</sup> <https://healpy.readthedocs.org/en/latest/>

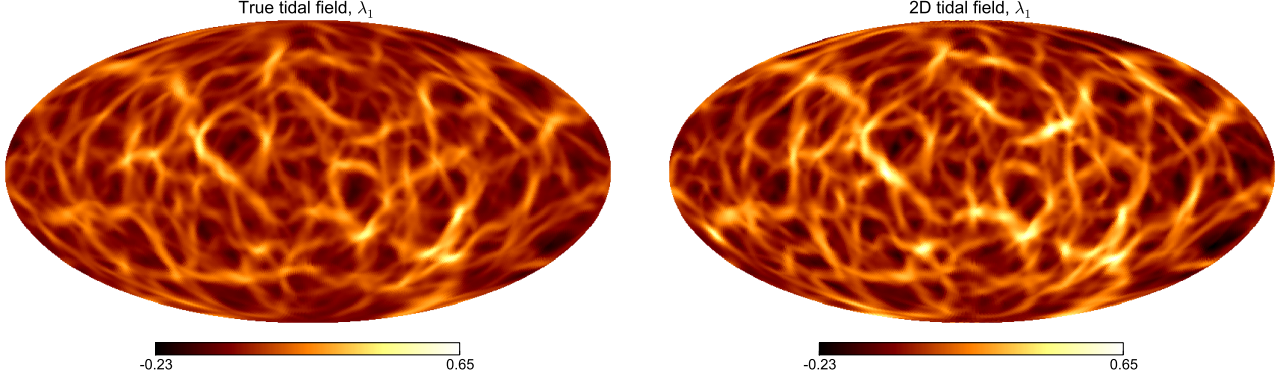


**Figure 4.** *Left panel:* principal eigenvalue of the true projected tidal field in our N-body simulation. *Right panel:* principal eigenvalue of the 2D tidal field measured from the corresponding mock galaxy catalog. A Gaussian smoothing kernel with  $\theta_s = 2^\circ$  was used in both cases. As discussed in Section 2.2.2, the 2D tidal field can be interpreted as a biased version of the true tidal field for most scales of interest.

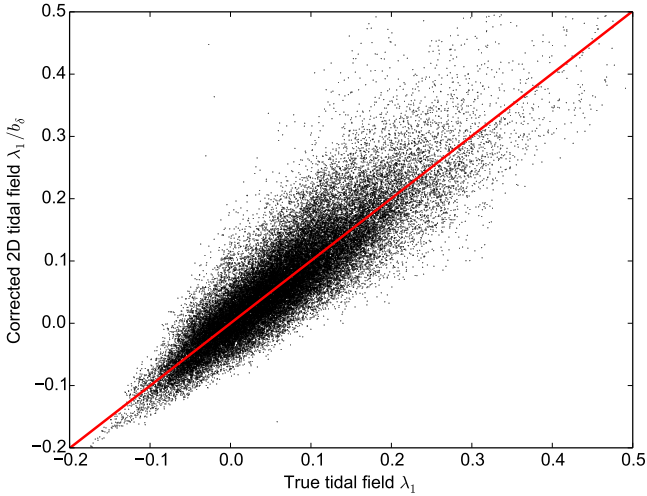


**Figure 5.** Two-dimensional distribution of the values of the principal eigenvalue  $\lambda_1$  of the true projected tidal tensor (x-axis) and the 2D tidal tensor (y-axis) scaled by the density bias  $b_\delta$ .  $b_\delta$  was found by fitting the analogous distribution in the plane of projected matter overdensity ( $\delta_M$ ) and projected galaxy overdensity ( $\delta_g$ ) to the model  $\delta_g = b_\delta \delta_M$ . The red solid line shows the best-fit linear regression, which corresponds to a slope of  $1.003 \pm 0.002$ , with a correlation coefficient  $r \sim 0.9$ , similar to the correlation coefficient found in the plane  $\delta_M - \delta_g$ .

environments defined in Section 2.2.3 (void, nexus and knot) for a given eigenvalue threshold  $\lambda_{th}$ .

Figure 2 shows the main products of this process. The top left panel shows a full-sky map of the density field smoothed with a  $1^\circ$  kernel used to infer the 2D tidal tensor. The environment classification derived from this tidal tensor, using the fiducial eigenvalue threshold quoted in Section 4.2 is shown in the top right panel. Finally, the two bottom panels show full-sky maps of the two eigenvalues of the 2D tidal tensor.

For this dataset, Figure 3 shows the fraction of the sky classified as each of the three environments as a function of the eigenvalue threshold  $\lambda_{th}$  for  $1^\circ$  (left panel) and  $5^\circ$  (right panel) Gaussian smoothing kernels. The figure also shows

the prediction from Gaussian theory outlined in Appendix B in both cases. The  $1^\circ$ -smoothed density field is clearly non-Gaussian and therefore the sky fractions are only in rough agreement with the Gaussian theory. After filtering out the smallest scales, responsible for most of the non-Gaussianity, we find that the Gaussian theory is able to describe the statistics of the projected cosmic web reasonably well for the  $5^\circ$ -smoothed field.

### 3.3 Connection with the projected tidal field

By using the true matter distribution available in the N-body simulation used to generate the mock galaxy catalog we can test in practice the relation between the 2D tidal field and the true projected tidal forces as described in Section 2.2.2. In order to do this we have carried out the following exercise:

- We first construct the three-dimensional density field of the simulation by interpolating the matter particles onto a Cartesian grid using cloud-in-cell interpolation. This was done using a grid with 512 grid points per dimension, corresponding to a resolution  $\Delta x = 1.37 \text{ Mpc}/h$ . We replicate this density grid in the three dimensions as described in section 3.1 to cover the volume of 2MASS.
- At each grid point we compute the value of the 3D tidal field by inverting Poisson's equation. Then, placing the observer at the centre of the simulated volume, we compute the transverse (angular) components of the 3D tidal field, as defined by the observer, by performing the corresponding three-dimensional rotation.
- We define a number  $N_z$  of angular pixel maps at different redshifts sampling the volume covered by 2MASS. For this we used  $N_z = 1024$  maps uniformly distributed in the range  $z \in [0, 0.3]$ , each of them with an angular resolution HEALPix parameter  $N_{side} = 1024$ . The values of  $T_{ab}$  computed in the Cartesian grid are then interpolated onto these spherical maps using trilinear interpolation. The high angular and radial resolution of the maps ( $\Delta x_{||} \simeq 0.82 \text{ Mpc}/h$ ,  $\Delta x_{\perp} < 0.8 \text{ Mpc}/h$ ) guarantees that essentially no information is lost in the process.
- The projected tidal tensor is then estimated by performing a weighted average over the  $N_z$  maps with weights

corresponding to the survey redshift distribution:

$$\hat{t}_p = \frac{\sum_{i=1}^{N_z} n(z_i) \hat{T}_p^{(i)}}{\sum_{i=1}^{N_z} n(z_i)}, \quad (20)$$

where  $\hat{T}_p^{(i)}$  are the transverse components of the 3D tidal tensor in the  $i$ -th pixel map at pixel  $p$ , and  $n(z_i)$  is the number of galaxies found in the  $i$ -th redshift bin.

The projected tidal field thus computed can then be compared with the 2D tidal tensor estimated from the mock galaxy catalog as described in section 3.2. Figure 4 shows the full-sky maps of the largest eigenvalue of both tensors for a smoothing scale  $\theta_{\text{sm}} = 2^\circ$ . The result supports the physical interpretation described in Section 2.2.2: at most scales of interest the 2D tidal tensor is a biased representation of the projected tidal forces, with the bias factor corresponding to the bias of the galaxy sample used to compute it.

In order to prove this quantitatively we have carried out the following exercise: we first compare the values of the projected galaxy overdensity field  $\delta_g$  and the true projected matter overdensity  $\delta_M$ , computed by averaging the three-dimensional matter overdensity in the simulation along the line of sight. From these data we estimate the density bias  $b_\delta$  by fitting a linear model  $\delta_g = b_\delta \delta_M$ , finding a best-fit value  $b_\delta = 1.15$  with a correlation coefficient  $r = 0.9$ . We then rescale the principal eigenvalue of the 2D tidal tensor in the simulation by  $b_\delta$  and compare the result with the principal eigenvalue of the true projected tidal tensor computed as described above. The result is shown in Figure 5, where the black dots correspond to the pairs of values found in the simulation, and the solid red line is the best-fit zero-intercept linear regression of the points. This fit yields a slope  $1.003 \pm 0.002$ , compatible with 1, and a correlation coefficient  $r = 0.88$ , similar to the value found for the overdensity field.

### 3.4 Dealing with an incomplete sky coverage

Even though the 2MASS catalog covered the whole celestial sphere, the Milky way covers a significant fraction of it, through which the density of detected sources is severely biased by star obscuration and dust extinction. These areas, as well as any region dominated by other observational systematics must therefore be discarded from the analysis, which complicates the application of the method presented here. The main difficulty lies in computing the 2D potential and its derivatives in an incomplete sky: as explained in the previous section, both operations are performed in harmonic space, which involves computing harmonic coefficients of incomplete maps that could be potentially biased. Even solving both problems in real space (e.g. solving Poisson's equation using relaxation techniques) would require assuming something about the values of the density field in the masked pixels, which could catastrophically bias the estimate of the 2D tidal tensor.

In this work we have studied two different methods to deal with these issues, which we describe here:

Method I: The overdensity field that we smooth and then use to compute the 2D potential is simply the masked overdensity field, with all masked pixels set to zero.

Method II: In this case we try to make use of constrained Gaussian realizations (CR from here on) in order to infer

the most likely value of the density field in the masked pixels based on the information we have about it outside the mask. Gaussian constrained realizations are used routinely in CMB experiments to simplify the computation of the angular power spectrum of maps with small masked areas in them. We will outline the basic procedure used for generating them here, and the reader is referred to Eriksen et al. (2004) for further details.

Writing the full-sky map of the observed density field as a vector  $\mathbf{d}$  with  $n_{\text{pix}}$  elements, we can separate it into uncorrelated signal and noise components,  $\mathbf{d} = \mathbf{s} + \mathbf{n}$ , where unseen (masked) pixels can be modelled as having a very large (infinite) noise component. Assuming both  $\mathbf{s}$  and  $\mathbf{n}$  to be Gaussianly distributed, it is easy to prove that the posterior probability distribution for the signal given the data is given by a multivariate normal distribution

$$p(\mathbf{s}|\mathbf{d}) = N(\mathbf{m}, \hat{C}), \quad (21)$$

with mean and covariance given by:

$$\mathbf{m} = (\hat{S}^{-1} + \hat{N}^{-1})^{-1} \hat{N}^{-1} \mathbf{d} \quad (22)$$

$$\hat{C} = (\hat{S}^{-1} + \hat{N}^{-1})^{-1}, \quad (23)$$

where  $\hat{S} \equiv \langle \mathbf{s} \mathbf{s}^T \rangle$  and  $\hat{N} \equiv \langle \mathbf{n} \mathbf{n}^T \rangle$  are the signal and noise covariance matrices (note that the mean  $\mathbf{m}$  corresponds to a Wiener-filtered version of the data). In our case we assume that the noise is white (i.e.  $\hat{N}$  is diagonal) and we mimic the effect of the mask by making the noise variance infinite in the masked pixels. The inverse noise matrix  $\hat{N}^{-1}$  is then easy to calculate in real space and is equal to the inverse noise variance in unmasked pixels and 0 in the masked ones. On the other hand the signal covariance  $\hat{S}$  is given by the two-point correlation function, which makes  $\hat{S}^{-1}$  easy to calculate in harmonic space, where it is diagonal. We can then find a maximum likelihood estimator (MLE) for the signal given the data as the mean of the probability distribution above (Eq. 22). Thus, the combined inverse covariance  $(\hat{S}^{-1} + \hat{N}^{-1})^{-1}$  needed to compute  $\mathbf{m}$  is not diagonal in either real or harmonic space, and the MLE estimator must be computed by numerically solving the linear system:

$$(\hat{S}^{-1} + \hat{N}^{-1}) \mathbf{m} = \hat{N}^{-1} \mathbf{d}. \quad (24)$$

For this we use the conjugate gradients method, using  $\hat{S}$  as a preconditioner.

Finally, we must note that the action of the signal inverse covariance  $\hat{S}^{-1}$  was computed by multiplying by the inverse power spectrum of the data in harmonic space. This was estimated as a polynomial fit in logarithmic space to the angular power spectrum of the data computed from the masked overdensity field as

$$C_\ell = \frac{\sum_{m=-\ell}^{\ell} |\tilde{a}_{\ell m}|^2}{(2\ell + 1) f_{\text{sky}}}, \quad (25)$$

where  $\tilde{a}_{\ell m}$  are the harmonic coefficients of the masked overdensity field (i.e. with all masked pixels set to zero) and  $f_{\text{sky}}$  is the fraction of unmasked sky<sup>4</sup>.

<sup>4</sup> Although this is, in general known to be a biased estimator of the angular power spectrum for incomplete skies, we verified that the resulting power spectrum was in good agreement with the one estimated using more sophisticated algorithms (e.g. Chon et al. (2004)).



	Method I	Method II
$\langle \Sigma_\lambda \rangle$	0.074	0.067
% area with $\Sigma_\lambda > 0.1$	16.4%	13.3%
% area with $\Sigma_\lambda > 0.2$	7.0%	5.9%
% missclassifications	5.2%	4.7%

**Table 1.** Comparison between the two methods used to deal with the mask. Even though both methods show very similar results, Method II outperforms the other two in the four different metrics, and was therefore our choice in the treatment of the real data.

The assumption that the signal, noise and data are Gaussianly distributed is not correct for the projected overdensity field, especially at low redshifts. In order to ameliorate this problem, we first transformed the original overdensity field ( $\delta_{\text{data}}$ ) into a “Gaussianized” version of it given by

$$\delta_{\text{Gaussian}} = \ln \left[ (1 + \delta_{\text{data}}) \sqrt{1 + \sigma_\delta^2} \right], \quad (26)$$

where  $\sigma_\delta^2 \equiv \langle \delta_{\text{data}}^2 \rangle$ . Since the overdensity field is known to be qualitatively well described by a lognormal distribution [Coles & Jones \(1991\)](#) (at least at the one-point level), the idea behind this operation is to produce a more Gaussian field by performing an inverse lognormal transformation on the original one.  $\delta_{\text{Gaussian}}$  and its power spectrum are then used to generate the MLE constrained realization, which is then transformed into a physical overdensity by inverting [Eq. 26](#).

Before ending this description, it is worth noting that this procedure yields the maximum-likelihood estimate of the tidal field inside the mask. We can then quantify the errors on this estimate by sampling from the posterior distribution and computing the standard deviation of the samples. Each sample can be drawn by generating two white Gaussian random fields with unit variance,  $\mathbf{r}_S$  and  $\mathbf{r}_N$ , and solving the modified linear system

$$(\hat{S}^{-1} + \hat{N}^{-1})\mathbf{s} = \hat{N}^{-1}\mathbf{d} + \hat{S}^{-1/2}\mathbf{r}_S + \hat{N}^{-1/2}\mathbf{r}_N. \quad (27)$$

We will use this method to compute the errors in our estimate of the 2D tidal field for the 2MASS galaxy survey.

Both for generating constrained realizations and for the calculation of the tidal tensor we make extensive use of direct and inverse spherical harmonic transforms (SHTs). Unlike in the case of Fourier transforms, direct and inverse SHTs do not cancel each other exactly, and small numerical errors can be generated if many consecutive transforms are applied to a given map, especially towards the poles of the sphere. Although we have verified that these errors are sufficiently small to be almost negligible for our purposes, we have tried to further minimize their effect by using angular coordinates such that the masked areas around the galactic plane occupy the regions close to the poles of our coordinate system, where these errors can be most relevant. Thus, all maps displayed below were shown in galactic coordinates rotated by 90 degrees (i.e., the galactic plane runs vertically through the centre of our maps leaving the North and South Galactic Poles to the left and right respectively).

In order to evaluate the goodness of both methods we have applied them to our simulated catalog using the angular mask employed in the analysis of the 2MASS data (see [Section 4.1](#)). We then compare the recovered 2D tidal ten-

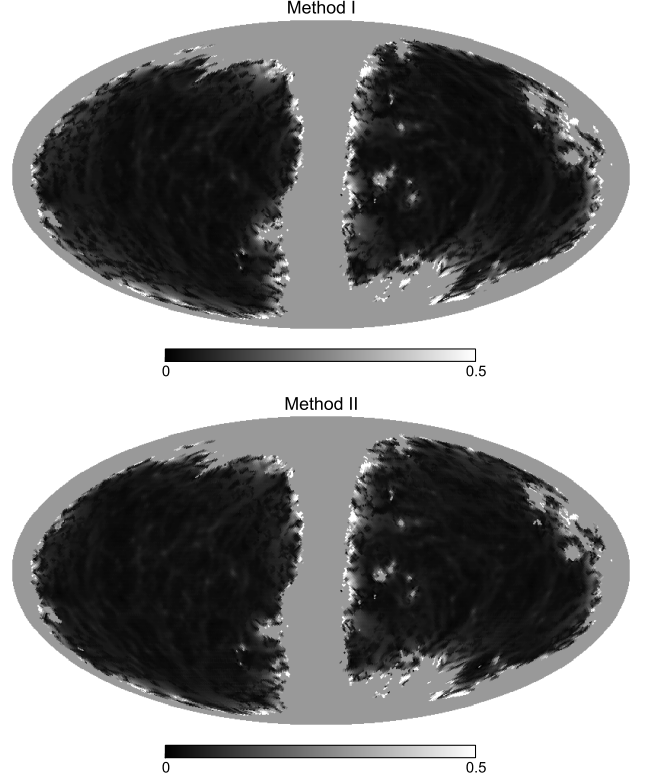


**Figure 6.** Maps of the error in the eigenvalues of the 2D tidal tensor in each pixel for the two methods described in [Section 3.4](#) to account for the incomplete sky coverage. This uses the simulations described in the text, with the low-latitude mask used for 2MASS, described in [Section 4.1](#). Method II gives smaller errors overall, and we use it as our method of choice for the analysis of the 2MASS data.

sor with the true tidal tensor computed without the angular mask. For each method we compute a map containing, for each pixel, the relative error in the estimated tidal tensor eigenvalues, defined as

$$\Sigma_\lambda = \sqrt{\frac{(\lambda_1^t - \lambda_1^r)^2 + (\lambda_2^t - \lambda_2^r)^2}{\langle (\lambda_1^t)^2 + (\lambda_1^r)^2 \rangle}}, \quad (28)$$

where  $\lambda_i^t$  is the true  $i$ -th eigenvalue (i.e. computed from the unmasked density field), and  $\lambda_i^r$  is the one recovered from the masked map. The ensemble average in the denominator was computed by summing over all pixels in the true map. We then judged the performance of each method by comparing four quantities: the average  $\Sigma_\lambda$  across the sky, the fraction of the sky where  $\Sigma_\lambda > 0.2$  and  $\Sigma_\lambda > 0.1$  and the fraction of pixels for which the environment type differs from the one found for the true map. We carried out this exercise for our fiducial smoothing scale and eigenvalue threshold ( $1^\circ$  and  $\lambda_{\text{th}} = 0.05$ ).

Figure 6 shows maps of  $\Sigma_\lambda$  for the three methods, and the quantitative results are summarized in [Table 1](#). Overall the best performance is achieved by method II. We observe a mild improvement with respect to method I due to the ability of the maximum-likelihood constrained realization to infer the value of the density field in the pixels near the edge of the mask, and therefore we used that method in the analysis of the 2MASS data.

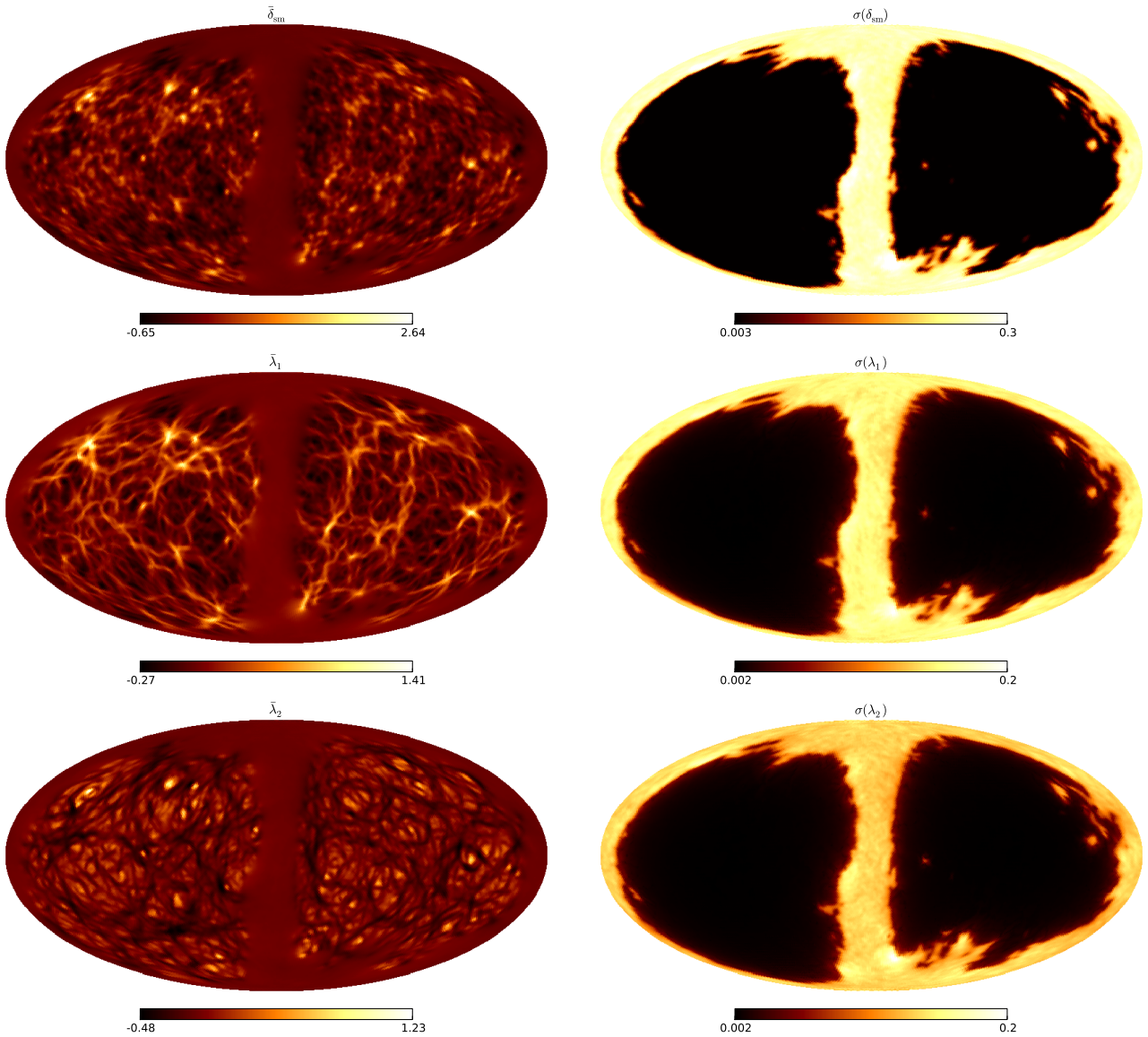


**Figure 7.** Mean (left column) and standard deviation (right column) of the projected smoothed galaxy density (upper panels) and the corresponding eigenvalues of the 2D tidal tensor (middle and lower panels) as estimated from 1000 constrained realizations of the 2MASS galaxy distribution. Note that the density field is basically unconstrained on masked regions distant from the mask edges, and therefore the mean of the constrained realizations is close to 0 there. A Gaussian smoothing kernel with standard deviation  $\theta_s = 1^\circ$  was used.

#### 4 THE COSMIC WEB OF 2MASS

In this section we describe our analysis of the projected tidal structure of the 2MASS survey, which we use to produce a map of the projected tidal forces in the local Universe. As an application of these results, we further study the environmental dependence of the galaxy luminosity function.

##### 4.1 The 2MASS galaxy survey

The Two-Micron All Sky Survey (2MASS) is a ground-based survey that was carried out between 1997 and 2001 using two twin telescopes located at Mount Hopkins, Arizona and Cerro Tololo, in Chile. It imaged practically the full celestial

sphere in the three photometric NIR bands  $J$ ,  $H$  and  $K_s$ <sup>5</sup>. The galaxy catalog used for our analysis is based on the 2MASS extended source catalog (XSC), containing 1647599 sources, of which more than 98% are galaxies, the remaining 2% being mainly galactic diffuse objects. Of these sources, we omitted all visually confirmed non-extended Galactic sources (flag  $\text{vc} = 2$ ), artifacts ( $\text{cc\_flag} = \text{a, z}$ ), duplicates ( $\text{use\_src} \neq 1$ ) and all objects with erroneous or excessively high  $J$ ,  $H$  or  $K_s$  magnitudes, resulting in a sample containing 1428756 objects<sup>6</sup>. In the analysis of this sample we

<sup>5</sup> All quoted apparent magnitudes correspond to the Vega magnitude system

<sup>6</sup> Note that this procedure very closely follows the method used by (Bilicki et al. 2014) to produce the 2MASS photometric redshift survey.

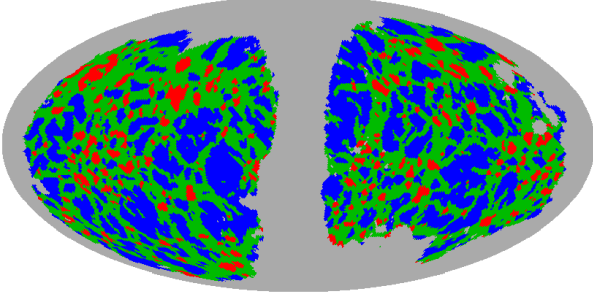


**Figure 8.** Tidal classification into voids (blue), nexuses (green) and knots (red) of the 2MASS density field. This classification is based on the  $1^\circ$ -smoothed maps of the tidal field eigenvalues shown in Figure 7, with a threshold  $\lambda_{th} = 0.05$ .

used the  $K_s$ -band 20 mag/arcsec<sup>2</sup> isophotal fiducial elliptical aperture magnitude (`k_m_k20fe`), which was corrected for Galactic extinction as

$$K_s \rightarrow K_s - A_K, \quad (29)$$

where the  $K_s$ -band correction  $A_K = 0.367 E(B - V)$  was computed from the dust reddening maps of [Schlegel et al. \(1998\)](#).

The main galaxy sample used in this analysis was selected with the aim of obtaining a complete and homogeneous sample. To that extent we followed the same procedures that were used in [Afshordi et al. \(2004\)](#); [Francis & Peacock \(2010\)](#); [Alonso et al. \(2015\)](#), which we summarize here. The two main sources of systematic incompleteness are dust extinction (quantified in terms of  $A_K$  above) and stars. We found that a complete and homogeneous sample can be selected for a limiting magnitude  $K_s = 13.9$  by cutting out all regions of the sky with either  $A_K \geq 0.06$  or  $\log_{10}(n_{\text{star}}/\text{deg}^2) \geq 3.5$ , where  $n_{\text{star}}$  is the counts of point sources brighter than  $K_s = 14$ . This procedure reduces the fraction of useable sky to about 69% and constitutes our main galaxy sample, containing 746733 of the 983963 galaxies with  $K_s \leq 13.9$ .

## 4.2 Results

### 4.2.1 Estimating the 2D tidal tensor

We estimate the 2D tidal tensor for the galaxy sample described above using Method II outlined in Section 3.4. In this approach we generate a suite of 1000 constrained lognormal realizations of the projected galaxy density field compatible with its statistics in the unmasked regions. Each of these realizations is generated with a HEALPix resolution `nside` = 64 and further smoothed using a Gaussian kernel with standard deviation  $\theta_{\text{sm}} = 1^\circ$ . The smoothed density field is then used to estimate the 2D tidal tensor as well as its eigenvalues and eigenvector in each realization as outlined in Section 3.2. We use this ensemble of estimated 2D tidal fields to evaluate the uncertainty in the measurement of  $\hat{t}$ . Figure 7 shows the mean (left column) and standard deviation (right column) of the smoothed density field (upper panels) and the major and minor eigenvalues of the 2D tidal tensor (middle and lower panels) computed from the constrained realizations.

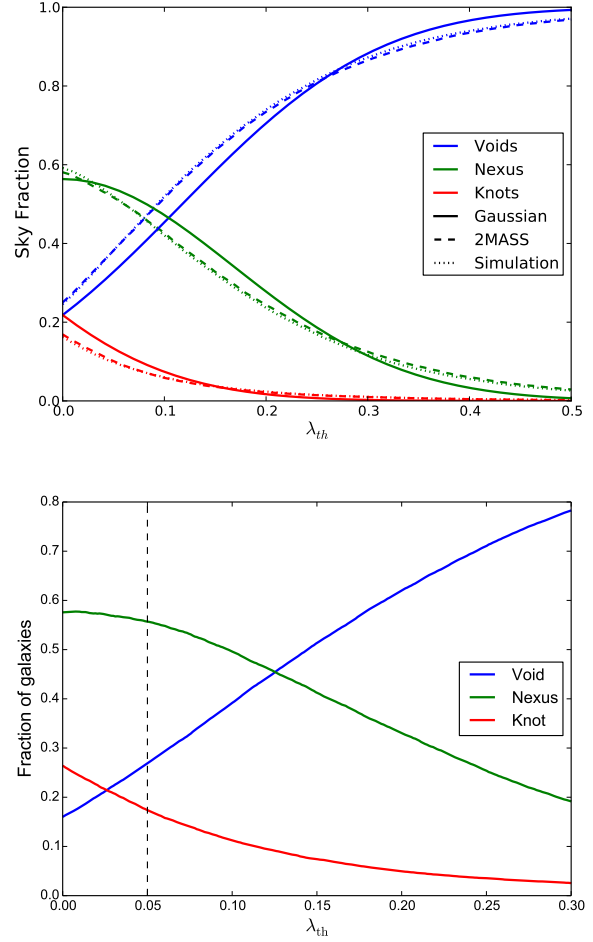


**Figure 9.** *Top panel:* sky fraction in the different environments for the 2MASS sample (dashed lines) compared with the simulated catalog (dotted lines) and the Gaussian theoretical prediction (solid lines) as a function of the eigenvalue threshold and for a smoothing scale  $\theta_s = 1^\circ$ . Blue, green and red lines correspond to voids, nexuses and knots respectively. Note that the level of disagreement with respect to the Gaussian theoretical prediction is similar to that shown in Fig. 3. *Bottom panel:* fraction of galaxies in the 2MASS sample found in the three different environments as a function of the eigenvalue threshold. The vertical dashed line shows our choice of  $\lambda_{th}$ .

The uncertainty in the determination of  $\hat{t}$  is very small in regions far from the mask edges, and grows sharply as they are approached. Knowing this uncertainty allows us then to define the regions where we trust that estimate enough for the subsequent analyses. We have thus computed the following quantity at each pixel:

$$\tilde{\Sigma}(\hat{\mathbf{n}}) = \sqrt{\frac{\sigma^2[\lambda_1(\hat{\mathbf{n}})] + \sigma^2[\lambda_2(\hat{\mathbf{n}})]}{\langle \bar{\lambda}_1^2 + \bar{\lambda}_2^2 \rangle_m}}, \quad (30)$$

where  $\sigma[\lambda_i(\hat{\mathbf{n}})]$  is the uncertainty in the  $i$ -th eigenvalue computed from the constrained realizations and  $\langle \dots \rangle_m$  implies averaging over all unmasked pixels.  $\tilde{\Sigma}$  quantifies the magnitude of the error on the tidal tensor eigenvalues normalized by their typical value. In all subsequent analyses, only regions not discarded by the mask described in Section 4.1,

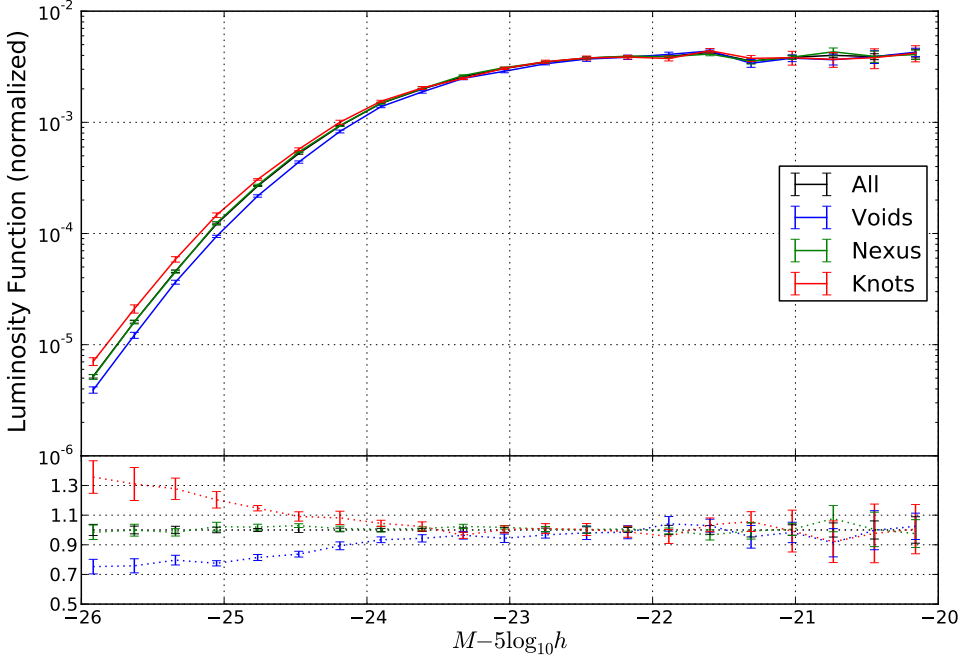


**Figure 10.** Luminosity function of the three environments shown in logarithmic scale. In the bright end we see a significant overabundance of galaxies in knots with respect to voids as predicted by the standard models of galaxy formation. The color code is voids (blue); nexuses (green); knots (red). The luminosity functions shown here were normalized to have the same amplitude on magnitudes  $M - 5 \log_{10} h > -23$ . The bottom panel shows the ratios of the void, nexus and knot LFs to the overall LF.

and for which  $\tilde{\Sigma} < 0.2$  were used, which reduced the available fraction of the sky to 65%. We will use this combined mask in all subsequent analyses unless otherwise stated.

#### 4.2.2 Statistics of the cosmic web

As described in Section 2.2.3, our measurement of the 2D tidal field can be used to define different types of environments in terms of the number of eigenvalues found above a given threshold  $\lambda_{\text{th}}$ . For this we use  $\lambda_{\text{th}} = 0.05$ , which we determined by dividing the 2MASS galaxy sample as equally as possible between environments (see Section 2.2.3 and the bottom panel of Fig. 9). The environment classification thus found for 2MASS, using the 2D tidal tensor averaged over the 200 constrained realizations, is shown in Figure 8.

In order to test the agreement of the statistics of the recovered tidal field with our theoretical expectations we have compared the sky fraction occupied by the different environments as a function of  $\lambda_{\text{th}}$  with the results from our simulated galaxy catalog and the theoretical Gaussian prediction outlined in Appendix B, as shown in Figure 9. The sky fractions recovered from the data agree well with the results from the simulated catalog and, qualitatively, follow the same trend predicted by the Gaussian theory. However, the agreement with the latter is much poorer, due to the non-Gaussian nature of the density field on small scales.

#### 4.2.3 Environmental Dependence of Luminosity Function

Having access to information about the tidal forces allows us, among other things, to study their influence in the process of galaxy formation and evolution. As an example of this kind of application we have studied the dependence of the luminosity function (LF) on the type of tidal environment. It is well known that more luminous galaxies tend to reside in the highest density regions of the Universe, however no clear dependence has yet been found on tidal or dimensional properties of the environment [Eardley et al. \(2015\)](#). In order to test this standard prediction in the context of the projected cosmic web, and to further search for other types of environmental dependence we have estimated the  $K_s$ -band luminosity function of 2MASS galaxies in knots, nexuses and voids.

Given the redshift  $z$  and apparent magnitude  $m$  of a galaxy, its absolute magnitude can be computed as

$$M = m - 5 \log_{10} \left[ \frac{d_L(z)}{1 \text{ Mpc}} \right] - 25 + K(z) + E(z), \quad (31)$$

where  $d_L(z) \equiv (1+z)\chi(z)$  is the luminosity distance and  $K(z)$  and  $E(z)$  are the  $k$ -correction and evolution correction respectively. For the  $K_s$ -band luminosity of 2MASS galaxies we use the simple forms  $K(z) = -6 \log_{10}(1+z)$  [Kochanek et al. \(2001\)](#) and  $E(z) = z$  [Blanton et al. \(2003\)](#), which are accurate enough at the low redshifts ( $z \lesssim 0.3$ ) covered by the survey. For this exercise we used a sample of 114930 galaxies with spectroscopic redshifts measured by SDSS [Eisenstein et al. \(2011\)](#) and the 2MASS redshift survey [Huchra et al. \(2012\)](#). This sample covers about 5000 square degrees



at galactic latitudes  $b \gtrsim 60^\circ$  with a spectroscopic completeness above 90% for  $K_s < 13.9$  (with the remaining 10% not showing any particular bias in magnitude or position). This sample was used in the calibration of the 2MPZ survey [Bilicki et al. \(2014\)](#), and the spectroscopic redshifts used here were obtained from their publicly available catalog.

Since the LF  $\phi(M)$  is the number density of galaxies per unit interval of absolute magnitude  $M$ , the probability of finding the  $i$ -th galaxy with absolute magnitude  $M_i$  given its redshift  $z_i$  in a magnitude-limited sample is given by

$$p(M_i|z_i) = \frac{\phi(M_i)}{\int_{-\infty}^{M_{\text{lim}}(z_i)} \phi(M) dM}, \quad (32)$$

where  $M_{\text{lim}}(z)$  is the limiting magnitude at redshift  $z$  given the magnitude limit of the sample. The joint likelihood of the full sample is then given by the product of this quantity over all the galaxies in the sample. Thus, given a model for the luminosity function, we can find the best-fit parameters of the model by maximizing  $\mathcal{L}$ .

Although a Schechter function [Schechter \(1976\)](#) has often been advocated as a simple and accurate parametrization of the LF, we prefer to use a non-parametric model in order to directly study the environmental dependence as a function of luminosity. Thus our method of choice is the non-parametric step-wise maximum likelihood estimator introduced by [Efstathiou et al. \(1988\)](#) (EEP from here on). This method models the LF as a step-wise function in a number of magnitude bins,

$$\phi(M) = \sum_{n=1}^{N_{\text{bins}}} \phi_n W(M_n - M), \quad (33)$$

where  $W(M_n - M)$  is a top-hat function centered around  $M_n$  with a width  $\Delta M$ . Substituting this model in Eq. 32, we find that the maximum-likelihood parameters  $\phi_n$  must satisfy:

$$\phi_n = \frac{\sum_{m=1}^{N_{\text{bins}}} W(M_n - M_m)}{\sum_{i=1}^{N_g} \frac{H(M_{\text{lim}}(z_i) - M_n)}{\sum_{l=1}^{N_{\text{bins}}} \phi_l H(M_{\text{lim}}(z_i) - M_l)}}, \quad (34)$$

where  $H(x)$  is the integral of  $W(x)$ . Given an initial guess for the  $\phi_n$ 's this equation can then be solved iteratively.

In order to use sample with high signal-to-noise magnitudes, we only use galaxies brighter than  $K_s = 13.75$  which, after imposing the mask defined in section 4.2.1 leaves us with a sample of 92585 galaxies, 22613 of them in voids, 50427 in nexuses and 19545 in knots.  $\phi(M)$  was estimated in  $N_{\text{bins}} = 20$  magnitude bins in the range  $M - 5 \log_{10} h \in [-26, -20]$ , and the statistical errors of these measurements were computed using 10 random jackknife realizations of each galaxy subsample. These jackknife errors were found to be in good agreement with the Poisson uncertainties expected given the galaxy counts in each magnitude bin. Since we expect a smaller environmental dependence in the faint end of the LF, we fix the normalization of the luminosity function in each environment by matching its amplitude to that of the overall LF for magnitudes  $M - 5 \log_{10} h > -23$  in a  $\chi^2$ -sense.

The result of this exercise is displayed in Figure 10: the top panel shows the LF measured in each environment and overall, while the bottom one shows the ratio of the LF in each environment with respect to the measured values across

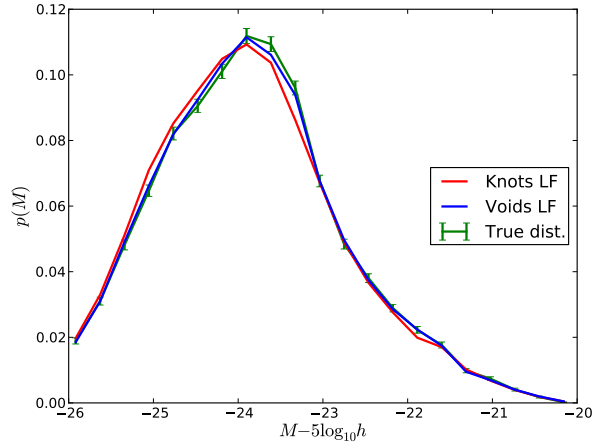


**Figure 11.** Magnitude distribution computed using the redshift of void galaxies and the EEP luminosity function estimated in voids (blue line), compared to the same quantity computed using the knots LF (but still using the void galaxy redshifts) (red line) and to the true magnitude distribution of void galaxies (green line with Poisson error bars). While the voids LF recovers the true magnitude distribution correctly, the distribution recovered using the knots LF shows significant disagreement. This confirms the statistical significance of the differences found between the luminosity function in voids and knots.

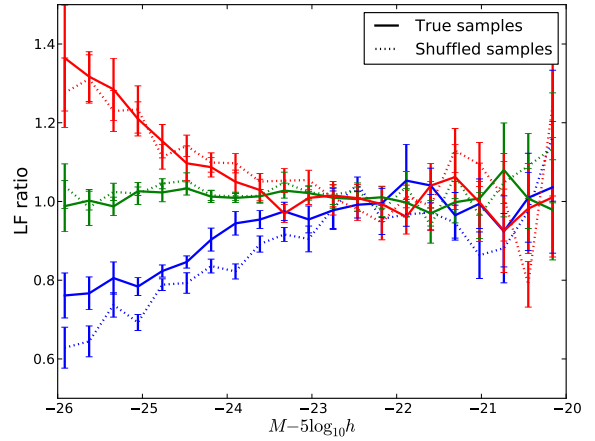


**Figure 12.** Ratio of the LFs for the true (solid lines) and shuffled (dotted lines) for voids (blue), nexuses (green) and knots (red), to the overall luminosity function. The true and shuffled samples show perfectly compatible luminosity functions, which support the idea that the differences between the three LFs is mainly due to the densities of the different environments, and not to their tidal structure.

the whole sky. We observe a significant increase in the number density of luminous galaxies in knots with respect to voids, while the nexus LF is perfectly compatible with the overall luminosity function across the whole range of luminosities. As a consistency check, and in order to verify the statistical significance of these differences we reconstructed the distribution of absolute magnitudes in the data from our estimates of the luminosity function, following [Sandage](#)

et al. (1979). To do this, we first compute, for each galaxy at redshift  $z_i$  in our sample, the conditional probability distribution  $p(M|z_i)$ , given in Eq. 32 in terms of the EEP luminosity function estimated for that sample. We then sum the distributions obtained for all galaxies, normalize the result to unity when integrated over magnitudes, and compare the result with the actual magnitude distribution of the data. The result is shown in Figure 11: the true magnitude distribution for void galaxies is nicely matched by that assuming the voids LF. However, if the luminosity function estimated for knots is used instead, the recovered distribution differs significantly from the true one, which confirms the difference between the two luminosity functions.

Although this is an interesting result, the fact that the three different environment types are associated with different density distributions (which are actually disjoint in the case of knots and voids), makes it difficult to ascertain whether these observed differences are caused by the tidal structure of the environment or merely by its local density, and there are theoretical and empirical reasons to presume that density is the dominant variable Alonso et al. (2015); Eardley et al. (2015). In order to address this question we have carried out an analysis similar to the one used in Eardley et al. (2015). We start by dividing our spectroscopic sample into bins of density. Then we generated shuffled galaxy samples for each environment type by substituting each galaxy residing in that environment by a random galaxy from the density bin in which it belongs (which will not in general come from the same environment type). We then compute the LF for these shuffled samples and compare them with the corresponding “true” LF for each environment type. Any differences between both LFs would then be entirely due to tidal effects independent of the environmental density. The result is shown in Figure 12: in all cases the LFs for the true and shuffled samples are perfectly compatible. Thus there is no evidence for a dependence of the LF on tidal effects beyond the density dependence.

## 5 DISCUSSION

In this paper we have presented a method to reconstruct the transverse tidal forces using the angular position of galaxies in a survey without reliable radial information. The method is based simply on adapting the standard Fourier methods used to estimate the tidal field in three-dimensional datasets to the two-dimensional sphere. We label the object thus recovered the “2D tidal tensor” and show, both in perturbation theory and using a simulated catalog, that for all scales of interest it can be interpreted as being proportional to the transverse components of the true tidal tensor averaged along the line of sight with the survey window function.

Since the method makes extensive use of operations in harmonic space, special care must be taken when dealing with incomplete sky coverage. In order to deal with this we make use of constrained lognormal realizations (as described in Section 3.4) in order to find a maximum-likelihood estimate of the tidal field and its uncertainty. We demonstrate the validity of this method by using it on a simulated galaxy catalog based on an N-body simulation. In doing so, we also show that the statistics of the recovered tidal field agree well with the Gaussian prediction (see Appendix B) on large

scales, although this agreement breaks down, as expected, on non-linear scales.

We then apply this method to the 2MASS survey and produce a full-sky map of the transverse tidal field, which we make publicly available<sup>7</sup>. The statistics of the recovered tidal field are found to agree quantitatively with our HOD-based simulated catalog and qualitatively with the Gaussian prediction.

Using the recovered tidal field we identify three different environment types (knots, nexuses and voids) based on the eigenvalues of the tidal tensor, and compute the luminosity function of galaxies located in each of them. We obtain statistically significant differences in the bright end of the LFs, finding an excess of luminous galaxies in knots with respect to voids. However, we show that this effect is most likely caused by the local density of the environment, and not by its tidal structure. This is in agreement with previous studies Eardley et al. (2015) and theoretical expectations Alonso et al. (2015).

Knowledge of the tidal field also has other interesting applications in cosmology. There is evidence of correlations between the intrinsic shapes and alignments of galaxies Blazek et al. (2011), which can be a major source of contamination for weak lensing studies. If those correlations were caused by the underlying tidal forces (as suggested by the non-linear alignment - NLA - model Catelan et al. (2001), as well as recent observations Pahwa et al. (2015)), prior knowledge about the projected tidal field could potentially reduce the effect of this systematic, effectively providing a prior on the contribution to the shear power spectrum from intrinsic alignments. Note that the projected tidal tensor (which we have shown is well approximated by the 2D tidal tensor) is precisely the quantity that gives rise to this contamination in the NLA model, and therefore the 2D tidal tensor could be used to test the validity of this model explicitly.

The method presented here could therefore be beneficial in the analysis of future deeper photometric surveys, such as DES The Dark Energy Survey Collaboration (2005) or LSST LSST Collaboration et al. (2009). A possible difficulty, in this case, would be the larger projection effects of samples deeper than the one used here, which could significantly degrade the signal-to-noise ratio of the recovered tidal field. A tomographic approach with sufficiently precise photometric redshifts would however ameliorate these effects, and allow for a study of the statistics of the tidal field as a function of redshift.

## ACKNOWLEDGMENTS

We would like to thank Maciej Bilicki, Elisa Chisari, Thibaut Louis and Sigurd Naess and for useful comments and discussions. DA is supported by BIPAC, ERC grant 259505 and the Oxford Martin School, and is grateful for the hospitality of Princeton University. BH acknowledges support from the Oxford Astrophysics Summer Student Programme.

<sup>7</sup> [http://intensitymapping.physics.ox.ac.uk/2mass\\_tidal.html](http://intensitymapping.physics.ox.ac.uk/2mass_tidal.html)

## REFERENCES

- Afshordi N., Loh Y.-S., Strauss M. A., 2004, *Phys. Rev. D*, 69, 083524, [arXiv:astro-ph/0308260](#)
- Alonso D., Eardley E., Peacock J. A., 2015, *MNRAS*, 447, 2683, [arXiv:1406.4159](#)
- Alonso D., Salvador A. I., Sánchez F. J., Bilicki M., García-Bellido J., Sánchez E., 2015, *MNRAS*, 449, 670, [arXiv:1412.5151](#)
- Appleby S., Shafieloo A., 2014, *JCAP*, 10, 70, [arXiv:1405.4595](#)
- Bardeen J. M., Bond J. R., Kaiser N., Szalay A. S., 1986, *ApJ*, 304, 15
- Berlind A. A., Weinberg D. H., 2002, *ApJ*, 575, 587
- Bilicki M., Jarrett T. H., Peacock J. A., Cluver M. E., Steward L., 2014, *ApJS*, 210, 9, [arXiv:1311.5246](#)
- Blanton M. R. et al., 2003, *ApJ*, 592, 819, [arXiv:astro-ph/0210215](#)
- Blazek J., McQuinn M., Seljak U., 2011, *JCAP*, 5, 10, [arXiv:1101.4017](#)
- Bond J. R., Myers S. T., 1996, *ApJS*, 103, 1
- Bond N. A., Strauss M. A., Cen R., 2010a, *MNRAS*, 406, 1609, [arXiv:0903.3601](#)
- Bond N. A., Strauss M. A., Cen R., 2010b, *MNRAS*, 409, 156, [arXiv:1003.3237](#)
- Carretero J., Castander F. J., Gaztañaga E., Crocce M., Fosalba P., 2015, *MNRAS*, 447, 646, [arXiv:1411.3286](#)
- Catelan P., Kamionkowski M., Blandford R. D., 2001, *MNRAS*, 320, L7, [arXiv:astro-ph/0005470](#)
- Chen Y.-C. et al., 2015, *ArXiv e-prints*, [arXiv:1509.06376](#)
- Choi E., Bond N. A., Strauss M. A., Coil A. L., Davis M., Willmer C. N. A., 2010, *MNRAS*, 406, 320, [arXiv:1003.3239](#)
- Chon G., Challinor A., Prunet S., Hivon E., Szapudi I., 2004, *MNRAS*, 350, 914, [arXiv:astro-ph/0303414](#)
- Coles P., Jones B., 1991, *MNRAS*, 248, 1
- del Castillo G. F. T., 2003, 3-D Spinors, Spin-Weighted Functions and their Applications. Birkhäuser
- Doroshkevich A. G., 1970, *Astrophysics*, 6, 320
- Eardley E. et al., 2015, *MNRAS*, 448, 3665, [arXiv:1412.2141](#)
- Efstathiou G., Ellis R. S., Peterson B. A., 1988, *MNRAS*, 232, 431
- Eisenstein D. J. et al., 2011, *AJ*, 142, 72, [arXiv:1101.1529](#)
- Eriksen H. K. et al., 2004, *ApJS*, 155, 227, [arXiv:astro-ph/0407028](#)
- Forero-Romero J. E., Contreras S., Padilla N., 2014, *MNRAS*, 443, 1090, [arXiv:1406.0508](#)
- Forero-Romero J. E., Hoffman Y., Gottlöber S., Klypin A., Yepes G., 2009, *MNRAS*, 396, 1815
- Francis C. L., Peacock J. A., 2010, *MNRAS*, 406, 2, [arXiv:0909.2494](#)
- Górski K. M., Hivon E., Banday A. J., Wandelt B. D., Hansen F. K., Reinecke M., Bartelmann M., 2005, *ApJ*, 622, 759, [arXiv:astro-ph/0409513](#)
- Hahn O., Porciani C., Carollo C. M., Dekel A., 2007, *MNRAS*, 375, 489
- Hirata C. M., Seljak U., 2004, *Phys. Rev. D*, 70, 063526, [arXiv:astro-ph/0406275](#)
- Hoffman Y., Metuki O., Yepes G., Gottlöber S., Forero-Romero J. E., Libeskind N. I., Knebe A., 2012, *MNRAS*, 425, 2049
- Huchra J. P. et al., 2012, *ApJS*, 199, 26, [arXiv:1108.0669](#)
- Jenkins A., Frenk C. S., White S. D. M., Colberg J. M., Cole S., Evrard A. E., Couchman H. M. P., Yoshida N., 2001, *MNRAS*, 321, 372
- Kochanek C. S. et al., 2001, *ApJ*, 560, 566, [arXiv:astro-ph/0011456](#)
- Lewis A., Challinor A., Lasenby A., 2000, *ApJ*, 538, 473, [arXiv:astro-ph/9911177](#)
- Libeskind N. I., Hoffman Y., Forero-Romero J., Gottlöber S., Knebe A., Steinmetz M., Klypin A., 2013, *MNRAS*, 428, 2489
- Libeskind N. I., Knebe A., Hoffman Y., Gottlöber S., 2014, *MNRAS*, 443, 1274, [arXiv:1407.0394](#)
- LSST Collaboration et al., 2009, *arXiv e-prints*, [arXiv:0912.0201](#)
- Metuki O., Libeskind N. I., Hoffman Y., Crain R. A., Theuns T., 2015, *MNRAS*, 446, 1458, [arXiv:1405.0281](#)
- Mo H. J., White S. D. M., 1996, *MNRAS*, 282, 347
- Nuza S. E., Kitaura F.-S., Heß S., Libeskind N. I., Müller V., 2014, *MNRAS*, 445, 988, [arXiv:1406.1004](#)
- Pahwa I. et al., 2015, *ArXiv e-prints*, [arXiv:1512.02236](#)
- Peacock J. A., Smith R. E., 2000, *MNRAS*, 318, 1144, [arXiv:astro-ph/0005010](#)
- Planck Collaboration et al., 2014, *A&A*, 571, A16, [arXiv:1303.5076](#)
- Sandage A., Tammann G. A., Yahil A., 1979, *ApJ*, 232, 352
- Schechter P., 1976, *ApJ*, 203, 297
- Schlegel D. J., Finkbeiner D. P., Davis M., 1998, *ApJ*, 500, 525, [arXiv:astro-ph/9710327](#)
- Sheth R. K., Tormen G., 1999, *MNRAS*, 308, 119
- Skrutskie M. F., et al., 2006, *ApJ*, 131, 1163
- Sousbie T., Pichon C., Colombi S., Novikov D., Pogosyan D., 2008, *MNRAS*, 383, 1655, [arXiv:0707.3123](#)
- Springel V., 2005, *MNRAS*, 364, 1105, [arXiv:astro-ph/0505010](#)
- The Dark Energy Survey Collaboration 2005, *ArXiv Astrophysics e-prints*, [arXiv:astro-ph/0510346](#)
- Vale A., Ostriker J. P., 2004, *MNRAS*, 353, 189, [arXiv:astro-ph/0402500](#)
- Yan H., Fan Z., White S. D. M., 2013, *MNRAS*, 430, 3432

## APPENDIX A: SPIN-S FUNCTIONS ON THE SPHERE

This section introduces a number of mathematical relations regarding spin- $s$  functions in  $S^2$  that will be useful in Appendices B and C.

Let us consider the unit 2-sphere embedded in  $\mathbb{R}^3$  and parametrized by the spherical coordinates  $(\theta, \varphi)$  as  $\mathbf{x} = (\sin \theta \cos \phi, \sin \theta \sin \phi, \cos \theta)$ . A rotation by an angle  $\psi \in [0, 2\pi)$  around a point  $\hat{\mathbf{n}}$  on the sphere is defined as a coordinate transformation such that directional vectors of the new coordinates  $(\theta', \varphi')$  are rotated with respect to the old ones by an angle  $\psi$  within the tangent plane at  $\hat{\mathbf{n}}$ .

Consider now a complex function defined on the unit sphere  $f(\hat{\mathbf{n}})$ . We say that  $f$  is a *spin- $s$  function* if its transformation law under rotations is  $f \rightarrow f' = e^{is\psi} f$ . Let us now define the so-called spin-raising and spin-lowering differential operators,  $\bar{\partial}$  and  $\partial$  respectively. They are defined

in terms of their actions on a spin- $s$  function  ${}_s f$ :

$$\tilde{\partial}_s f \equiv -(\sin \theta)^s (\partial_\theta + i \partial_\varphi / \sin \theta) (\sin \theta)^{-s} ({}_s f) \quad (\text{A1})$$

$$\bar{\partial}_s f \equiv -(\sin \theta)^{-s} (\partial_\theta - i \partial_\varphi / \sin \theta) (\sin \theta)^s ({}_s f). \quad (\text{A2})$$

It is possible to prove that, if  $f$  is a spin- $s$  function, then  $\tilde{\partial} f$  and  $\bar{\partial} f$  will be spin- $s+1$  and spin- $s-1$  quantities respectively (del Castillo 2003).

The simplest functions we can define on the sphere are scalar (spin-0) functions. Such functions can always be expanded in terms of the ordinary spherical harmonics:

$$f(\hat{\mathbf{n}}) = \sum_{\ell=0}^{\infty} \sum_{m=-\ell}^{\ell} f_{\ell m} Y_{\ell m}(\hat{\mathbf{n}}). \quad (\text{A3})$$

By applying the spin-raising and lowering operators we can define the so-called spin-weighted spherical harmonics  ${}_s Y_{\ell m}$ , defined as

$${}_s Y_{\ell m} \equiv \begin{cases} \sqrt{\frac{(\ell-s)!}{(\ell+s)!}} (\tilde{\partial}^s) Y_{\ell m} & 0 \leq s \leq \ell \\ (-1)^s \sqrt{\frac{(\ell+s)!}{(\ell-s)!}} (\bar{\partial}^{-s}) Y_{\ell m} & -\ell \leq s \leq 0 \\ 0 & \text{otherwise} \end{cases} \quad (\text{A4})$$

Spin- $s$  functions are then amenable to a harmonic expansion in terms of the spin- $s$  spherical harmonics  ${}_s Y_{\ell m}$ .

The spin-weighted spherical harmonics are related to the Wigner- $d$  rotation matrices through:

$${}_s Y_{\ell m}(\theta, \varphi) = (-1)^m \sqrt{\frac{2\ell+1}{4\pi}} e^{im\varphi} d_{-m s}^{\ell}(\theta). \quad (\text{A5})$$

The orthogonality of the Wigner- $d$  matrices ( $\sum_{m=-\ell}^{\ell} d_{ms}^{\ell} (d_{mr}^{\ell})^* = \delta_{sr}$ ) then implies the following useful relation for the spin-weighted spherical harmonics:

$$\sum_{m=-\ell}^{\ell} |{}_s Y_{\ell m}|^2 = \frac{2\ell+1}{4\pi}. \quad (\text{A6})$$

## APPENDIX B: GAUSSIAN STATISTICS OF THE 2D TIDAL TENSOR

This appendix discusses and derives the Gaussian prediction for the distribution of the 2D tidal field eigenvalues and the sky fraction occupied by the three different elements of the projected cosmic web.

As outlined in Section 2.2, the 2D tidal tensor is defined in terms of the projected galaxy overdensity as

$$\hat{t} \equiv \hat{H}(\nabla_{\hat{\mathbf{n}}}^{-2} \delta), \quad (\text{B1})$$

where  $\nabla_{\hat{\mathbf{n}}}^{-2} f$  denotes the particular solution of Poisson's equation on the 2-sphere with  $f$  as a source, and  $\hat{H}$  is the covariant Hessian defined in Eq. 6. We have further defined the 2D potential  $\phi \equiv \nabla_{\hat{\mathbf{n}}}^{-2} \delta$ , so that  $\hat{t} = \hat{H}\phi$ .

The 2D tidal tensor can also be written in closed form using the spin-raising and lowering operators  $\tilde{\partial}$  and  $\bar{\partial}$ , introduced in the previous section, as

$$\hat{H}\phi \equiv \frac{1}{2} \begin{pmatrix} \tilde{\partial}\bar{\partial}\phi + \text{Re}(\tilde{\partial}\bar{\partial}\phi) & \text{Im}(\tilde{\partial}\bar{\partial}\phi) \\ \text{Im}(\tilde{\partial}\bar{\partial}\phi) & \tilde{\partial}\bar{\partial}\phi - \text{Re}(\tilde{\partial}\bar{\partial}\phi) \end{pmatrix}. \quad (\text{B2})$$

The 2D tidal tensor can also be expressed in terms of the covariant derivatives on the sphere as

$$H_{ab}\phi = \frac{\nabla_a \nabla_b \phi}{|\mathbf{e}_a||\mathbf{e}_b|}, \quad (\text{B3})$$

where  $\nabla_a$  denotes the covariant derivative with respect to the coordinate  $q_a$  (either  $\theta$  or  $\varphi$ ), and  $\mathbf{e}_a \equiv \partial \hat{\mathbf{n}} / \partial q_a$  is the Vielbein of the 2-sphere.

Let us focus now on describing the 1-point statistics of the 2D tidal tensor under the assumption that the underlying overdensity field is Gaussian. In this case, the probability distribution for  $\hat{t}$  will be completely determined by the covariance of its elements:

$$C_{abcd} \equiv \langle t_{ab} t_{cd} \rangle = \frac{\langle \nabla_a \nabla_b \phi \nabla_c \nabla_d \phi \rangle}{|\mathbf{e}_a||\mathbf{e}_b||\mathbf{e}_c||\mathbf{e}_d|}. \quad (\text{B4})$$

Using the isotropy of the underlying overdensity field, as well as the symmetry properties of the indices ( $a \leftrightarrow b$ ,  $c \leftrightarrow d$ ,  $(a, b) \leftrightarrow (c, d)$ ), we can argue that the tensor in the numerator must be a linear combination of the only three 4-index isotropic tensors with equivalent symmetries:

$$\langle \nabla_a \nabla_b \phi \nabla_c \nabla_d \phi \rangle = \alpha g_{ab} g_{cd} + \beta g_{ac} g_{bd} + \gamma g_{ad} g_{cb}, \quad (\text{B5})$$

where  $g_{ab}$  is the metric of the 2-sphere.

Multiplying this expression above by  $g^{ab} g^{cd}$ ,  $g^{ac} g^{bd}$  and  $g^{ad} g^{cb}$ , and summing over all indices yields a linear system of three equations for the three unknown coefficients  $\alpha$ ,  $\beta$  and  $\gamma$ . Solving this system, we find that the covariance matrix can be written as

$$C_{abcd} = \frac{1}{8} [(3S_A - 2S_B) \delta_{ab} \delta_{cd} + (2S_B - S_A) (\delta_{ac} \delta_{bd} + \delta_{ad} \delta_{cb})], \quad (\text{B6})$$

where  $S_A$  and  $S_B$  are the only two second-order rotational invariants of  $\hat{t}$ :

$$S_A \equiv \langle [\text{Tr}(\hat{t})]^2 \rangle = \langle |\tilde{\partial}\bar{\partial}\phi|^2 \rangle, \quad (\text{B7})$$

$$S_B \equiv \langle \text{Tr}(\hat{t}^2) \rangle = \frac{1}{2} (\langle |\tilde{\partial}\bar{\partial}\phi|^2 \rangle + \langle |\bar{\partial}\tilde{\partial}\phi|^2 \rangle). \quad (\text{B8})$$

The two ensemble averages  $\langle |\tilde{\partial}\bar{\partial}\phi|^2 \rangle$  and  $\langle |\bar{\partial}\tilde{\partial}\phi|^2 \rangle$  can be computed using the harmonic expansion of  $\phi$ :

$$\phi(\hat{\mathbf{n}}) \equiv \sum_{\ell=0}^{\infty} \sum_{m=-\ell}^{\ell} \phi_{\ell m} Y_{\ell m}(\hat{\mathbf{n}}). \quad (\text{B9})$$

Using the definition of the spin-weighted spherical harmonics introduced in Appendix A we obtain:

$$\langle |\tilde{\partial}\bar{\partial}\phi|^2 \rangle = \sum_{\ell=0}^{\infty} C_{\ell}^{\phi} \left( \frac{(\ell+1)!}{(\ell-1)!} \right)^2 \sum_{m=-\ell}^{\ell} |{}_0 Y_{\ell m}|^2, \quad (\text{B10})$$

$$\langle |\bar{\partial}\tilde{\partial}\phi|^2 \rangle = \sum_{\ell=0}^{\infty} C_{\ell}^{\phi} \frac{(\ell+2)!}{(\ell-2)!} \sum_{m=-\ell}^{\ell} |{}_2 Y_{\ell m}|^2 \quad (\text{B11})$$

where we have defined the power spectrum of the 2D potential  $\langle \phi_{\ell m} \phi_{\ell' m'}^* \rangle \equiv C_{\ell}^{\phi} \delta_{\ell\ell'} \delta_{mm'}$ . Using the relation between the harmonic coefficients of the 2D potential and the projected density field ( $\delta_{\ell m} = -\ell(\ell+1)\phi_{\ell m}$ ) as well as the orthogonality relation (Eq. A6) we finally obtain:

$$\sigma_{\delta}^2 \equiv \langle |\tilde{\partial}\bar{\partial}\phi|^2 \rangle = \sum_{\ell=0}^{\infty} \frac{2\ell+1}{4\pi} C_{\ell}^{\delta}, \quad (\text{B12})$$

$$\tilde{\sigma}_{\delta}^2 \equiv \langle |\bar{\partial}\tilde{\partial}\phi|^2 \rangle = \sum_{\ell=0}^{\infty} \frac{2\ell+1}{4\pi} C_{\ell}^{\delta} \left[ \frac{(\ell+2)(\ell-1)}{\ell(\ell+1)} \right]. \quad (\text{B13})$$

Note that  $\sigma_{\delta}^2$  is the variance of the projected overdensity field. Furthermore, in the flat-sky approximation, where only



the highest multipoles ( $\ell \gg 1$ ) contribute to the total power,  $\tilde{\sigma}_\delta \simeq \sigma_\delta$ , and thus  $S_B \simeq S_A = \sigma_\delta^2$ .

Collecting the three independent terms of the 2D tidal tensor into a three-dimensional vector:  $\mathbf{t} \equiv (t_{\theta\theta}, t_{\phi\phi}, t_{\theta\phi})$ , the covariance matrix can be written as a  $3 \times 3$  symmetric matrix in terms of  $\sigma_\delta^2$  and  $\tilde{\sigma}_\delta^2$ :

$$\hat{C} \equiv \langle \mathbf{t} \mathbf{t}^T \rangle = \frac{1}{8} \begin{pmatrix} 2\sigma_\delta^2 + \tilde{\sigma}_\delta^2 & 2\sigma_\delta^2 - \tilde{\sigma}_\delta^2 & 0 \\ 2\sigma_\delta^2 - \tilde{\sigma}_\delta^2 & 2\sigma_\delta^2 + \tilde{\sigma}_\delta^2 & 0 \\ 0 & 0 & \tilde{\sigma}_\delta^2 \end{pmatrix}. \quad (\text{B14})$$

In order to derive the probability distribution for the eigenvalues of  $\hat{t}$ , we follow the procedure used in [Alonso et al. \(2015\)](#). The probability distribution for the vector  $\mathbf{t}$  is given by a multivariate Gaussian:

$$p(\mathbf{t}) \prod_{A=1}^3 dt_A = \frac{\exp \left[ -\frac{1}{2} \mathbf{t}^T \hat{C}^{-1} \mathbf{t} \right]}{\sqrt{(2\pi)^3 \det(\hat{C})}} \prod_A dt_A. \quad (\text{B15})$$

This can be simplified by defining the rescaled variables:

$$\nu \equiv \frac{t_1 + t_2}{\sigma_\delta}, \quad \rho \equiv \frac{t_1 - t_2}{2\tilde{\sigma}_\delta}, \quad \tau \equiv \frac{t_3}{\tilde{\sigma}_\delta}, \quad (\text{B16})$$

which diagonalize the covariance matrix, yielding

$$p(\mathbf{t}) \prod_{A=1}^3 dt_A = \frac{8 e^{-(\nu^2 + 8\rho^2 + 8\tau^2)/2}}{(2\pi)^{3/2} \sigma_\delta \tilde{\sigma}_\delta^2} \prod_A dt_A. \quad (\text{B17})$$

On the other hand, the volume element  $\prod_A dt_A$  in the space of  $2 \times 2$  symmetric matrices can be written in terms of their two eigenvalues,  $\lambda_1$  and  $\lambda_2$  and the angle defining the two-dimensional rotation that diagonalizes it [Bardeen et al. \(1986\)](#):

$$\prod_A dt_A = |\lambda_1 - \lambda_2| d\lambda_1 d\lambda_2 \frac{d\phi}{4}, \quad (\text{B18})$$

where the factor of  $1/4$  accounts for the two different orderings of the eigenvalues and the overall sign defines the orientation of the eigenvectors. Choosing the ordering  $\lambda_1 > \lambda_2$  introduces a factor of 2. Expressing  $\lambda_1$  and  $\lambda_2$  in terms of  $\nu$  and  $\rho$ , and integrating the irrelevant angular part, we finally obtain the distribution:

$$p(\nu, \rho) d\nu d\rho = 8\rho e^{-4\rho^2} d\rho \frac{e^{-\nu^2/2}}{\sqrt{2\pi}} d\nu \quad (\text{B19})$$

The ordering  $\lambda_1 > \lambda_2$  has the effect of reducing the dynamical range of  $\rho$  to  $\rho > 0$ , and the integration limits for  $\nu$  are determined by the environment type, defined by the eigenvalue threshold  $\lambda_{\text{th}}$  and the number of eigenvalues above the threshold ( $\alpha$ ). In general we can write  $f_1(\alpha, \rho) < \nu - \nu_{\text{th}} < f_2(\alpha, \rho)$ , with  $\nu_{\text{th}} \equiv 2\lambda_{\text{th}}/\sigma_\delta$  and

$$f_1(\alpha, \rho) = \begin{cases} -\infty & \alpha = 0 \text{ (void)} \\ -2\frac{\tilde{\sigma}_\delta}{\sigma_\delta}\rho & \alpha = 1 \text{ (nexus)} \\ 2\frac{\tilde{\sigma}_\delta}{\sigma_\delta}\rho & \alpha = 2 \text{ (knot)} \end{cases}, \quad (\text{B20})$$

$$f_2(\alpha, \rho) = \begin{cases} -2\frac{\tilde{\sigma}_\delta}{\sigma_\delta}\rho & \alpha = 0 \text{ (void)} \\ 2\frac{\tilde{\sigma}_\delta}{\sigma_\delta}\rho & \alpha = 1 \text{ (nexus)} \\ \infty & \alpha = 2 \text{ (knot)} \end{cases}. \quad (\text{B21})$$

The sky fraction for the three types of environment can then be computed by integrating the probability distribution in

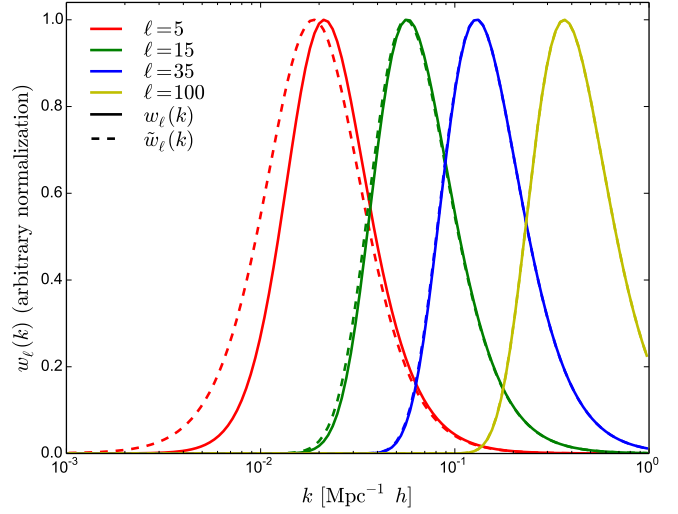


**Figure C1.** Window functions  $w_\ell(k)$  and  $\tilde{w}_\ell(k)$  defined in Equations C10 and C12 for the 2MASS selection function and different values of the multipole order  $\ell$ . The difference between the 2D tidal tensor and the projected tidal forces is effectively encapsulated in the differences between the two functions. These differences become negligible by  $\ell \simeq 15$ , and hence, for most scales of interest, it is safe to interpret the 2D tidal tensor as describing the transverse tidal forces averaged along the line of sight.

Eq. B19 with the corresponding integration limits for  $\nu$ :

$$F_V(\alpha, \lambda_{\text{th}}) = \frac{8}{\sqrt{2\pi}} \int_0^\infty d\rho \int_{\nu_{\text{th}} + f_1(\alpha, \rho)}^{\nu_{\text{th}} + f_2(\alpha, \rho)} d\nu \rho e^{-(\nu^2 + 8\rho^2)/2}. \quad (\text{B22})$$

Note that this integral can be solved analytically in terms of error functions, but we omit the resulting cumbersome expression.

## APPENDIX C: RELATION BETWEEN THE 2D TIDAL TENSOR AND THE PROJECTED TIDAL FORCES

Using the flat-sky approximation, we have shown in Section 2.2.2 that the 2D tidal tensor, as defined in Section 2.2.1 can be interpreted, on sufficiently small scales, as being proportional to the gravitational tidal forces in the transverse (angular) directions averaged along the line of sight with the survey selection function. The aim of this Appendix is to present a more rigorous proof of this relation in the full-sky limit, as well as to provide the formulas relating the 2D tidal tensor and the underlying matter perturbations.

As shown in Appendix B, the components of the 2D tidal tensor can be related to the two complex quantities

$$t^{(0)}(\hat{\mathbf{n}}) \equiv \bar{\partial}\bar{\partial} \left[ \nabla_{\hat{\mathbf{n}}}^{-2} \left( \int_0^\infty d\chi w(\chi) \delta^s(\chi \hat{\mathbf{n}}) \right) \right], \quad (\text{C1})$$

$$t^{(2)}(\hat{\mathbf{n}}) \equiv \bar{\partial}\bar{\partial} \left[ \nabla_{\hat{\mathbf{n}}}^{-2} \left( \int_0^\infty d\chi w(\chi) \delta^s(\chi \hat{\mathbf{n}}) \right) \right], \quad (\text{C2})$$

where  $\delta^s(\mathbf{x})$  is the observed density field in redshift space. On the other hand, the projected tidal tensor (i.e. the tidal forces along the transverse directions averaged along the line

of sight) is given by the analogous quantities:

$$\tilde{t}^{(0)}(\hat{\mathbf{n}}) \equiv \int_0^\infty d\chi w(\chi) \frac{\bar{\partial}\bar{\partial}\Phi(\chi\hat{\mathbf{n}})}{\chi^2}, \quad (\text{C3})$$

$$\tilde{t}^{(2)}(\hat{\mathbf{n}}) \equiv \int_0^\infty d\chi w(\chi) \frac{\bar{\partial}\bar{\partial}\Phi(\chi\hat{\mathbf{n}})}{\chi^2}, \quad (\text{C4})$$

where  $\Phi$  is the Newtonian potential normalized so that  $\nabla^2\Phi = \delta$ , with  $\delta$  the real-space density field. Let us focus, for the moment, on the trace of the two tidal tensors, given by  $t^{(0)}$  and  $\tilde{t}^{(0)}$ .

We start by computing the harmonic coefficients of both quantities, given by

$$t_{\ell m}^{(0)} \equiv \int d\hat{\mathbf{n}} Y_{\ell m}^*(\hat{\mathbf{n}}) t^{(0)}(\hat{\mathbf{n}}), \quad (\text{C5})$$

(and likewise for  $\tilde{t}^{(0)}$ ). We can relate  $t_{\ell m}^{(0)}$  to the matter density perturbations by doing the following:

- First, expand  $\delta_s$  in Eq. C1 in terms of its Fourier coefficients, and use the plane-wave expansion

$$e^{i\mathbf{k}\cdot\mathbf{x}} = \sum_{\ell=0}^{\infty} 4\pi i^\ell j_\ell(k\chi) \sum_{m=-\ell}^{\ell} Y_{\ell m}(\hat{\mathbf{n}}) Y_{\ell m}^*(\hat{\mathbf{n}}_k), \quad (\text{C6})$$

where  $\mathbf{x} \equiv \chi\hat{\mathbf{n}}$ ,  $\hat{\mathbf{n}}_k$  is the unit vector in Fourier space and  $j_\ell(x)$  is the order- $\ell$  spherical Bessel function of the first kind.

- Apply the operator  $\bar{\partial}\bar{\partial}\nabla_{\hat{\mathbf{n}}}^{-2}$  on the spherical harmonic  $Y_{\ell m}(\hat{\mathbf{n}})$

$$\bar{\partial}\bar{\partial}\nabla_{\hat{\mathbf{n}}}^{-2} Y_{\ell m}(\hat{\mathbf{n}}) = Y_{\ell m}(\hat{\mathbf{n}}) \quad (\text{C7})$$

- Relate the Fourier coefficients of the observed overdensity field  $\delta^s$  to the real-space density perturbations:

$$\delta_{\mathbf{k}}^s j_\ell(k\chi) \longrightarrow b \delta_{\mathbf{k}} [j_\ell(k\chi) - \beta j_\ell''(k\chi)], \quad (\text{C8})$$

where  $b$  is the linear galaxy bias and  $\beta$  is the redshift distortion parameter.

- Define the harmonic coefficients of  $\delta_{\mathbf{k}}$  as

$$\delta_{\ell m}(k) \equiv \int d\hat{\mathbf{n}}_k Y_{\ell m}^*(\hat{\mathbf{n}}_k) \delta_{\mathbf{k}}. \quad (\text{C9})$$

Finally we obtain the following relation between  $t_{\ell m}^{(0)}$  and  $\delta_{\ell m}(k)$ :

$$t_{\ell m}^{(0)} = b \frac{4\pi i^\ell}{(2\pi)^{3/2}} \int_0^\infty dk k^2 \delta_{\ell m} w_\ell(k), \quad (\text{C10})$$

with

$$w_\ell(k) \equiv \int_0^\infty d\chi [j_\ell(k\chi) - \beta j_\ell''(k\chi)] w(\chi). \quad (\text{C11})$$

Following analogous steps for  $\tilde{t}_{\ell m}^{(0)}$  yields a similar relation:

$$\tilde{t}_{\ell m}^{(0)} = \frac{4\pi i^\ell}{(2\pi)^{3/2}} \int_0^\infty dk k^2 \delta_{\ell m} \tilde{w}_\ell(k), \quad (\text{C12})$$

with

$$\tilde{w}_\ell(k) \equiv \int_0^\infty d\chi \frac{\ell(\ell+1)}{(k\chi)^2} j_\ell(k\chi) w(\chi). \quad (\text{C13})$$

Thus, as was shown in the flat-sky case, the differences between the 2D tidal tensor and the projected tidal forces, besides the linear galaxy bias acting as a proportionality constant, are encapsulated in the different window functions  $w_\ell$  and  $\tilde{w}_\ell$  above.

Figure C1 shows both window functions for different values of  $\ell$  for the 2MASS selection function using an RSD parameter  $\beta = 0.46$  (Alonso et al. 2015). As is evident, on small scales (large- $\ell$ ) both functions are almost equivalent, and in this case the 2D tidal tensor can be safely interpreted as describing the average tidal forces in the transverse directions.

Similar relations can be derived for  $t^{(2)}$  and  $\tilde{t}^{(2)}$  by following the same steps outlined above, with the exception that, since they are spin-2 quantities, their harmonic coefficients must be computed using the spin-weighted spherical harmonics (Eq. A4). The resulting expressions are

$$t_{\ell m}^{(2)} = b \frac{4\pi i^\ell}{(2\pi)^{3/2}} \int_0^\infty dk k^2 \delta_{\ell m} w_\ell^{(2)}(k), \quad (\text{C14})$$

$$\tilde{t}_{\ell m}^{(2)} = \frac{4\pi i^\ell}{(2\pi)^{3/2}} \int_0^\infty dk k^2 \delta_{\ell m} \tilde{w}_\ell^{(2)}(k), \quad (\text{C15})$$

with

$$\begin{pmatrix} w_\ell^{(2)}(k) \\ \tilde{w}_\ell^{(2)}(k) \end{pmatrix} \equiv \left[ \frac{(\ell+2)(\ell-1)}{\ell(\ell+1)} \right]^{1/2} \begin{pmatrix} w_\ell(k) \\ \tilde{w}_\ell(k) \end{pmatrix}. \quad (\text{C16})$$